



JACOBS  
UNIVERSITY

Dottorato in Scienze e Tecnologie Chimiche Ciclo XXVIII – PhD Degree in Biochemistry

**Structural and functional analysis of human voltage-dependent anion  
channel isoforms (hVDACs):**

**Combining in-vitro and in-silico approaches**

SSD: Chim/02

by

**Giuseppe Federico Amodeo**

Cordinatore:

Prof. Mariano Casu

Tutor:

Prof. Mariano Casu

Prof. Mathias Winterhalter

**Esame finale anno accademico 2014 – 2015**



# **1 Statutory Declaration**

(on Authorship of a Dissertation)

I, Giuseppe Federico Amodeo, hereby declare that I have written this PhD thesis independently, unless where clearly stated otherwise. I have used only the sources, the data and the support that I have clearly mentioned. This PhD thesis has not been submitted for conferral of degree elsewhere.

I confirm that no rights of third parties will be infringed by the publication of this thesis.

Bremen, April 7, 2016

## INDEX

<b>Acknowledgments</b>	<b>II</b>
<b>Chapter 1. Introduction</b>	<b>1</b>
<b>1.1 Aim of the PhD Thesis</b>	<b>5</b>
<b>Chapter 2. Methods</b>	<b>8</b>
<b>2.1 In-vitro Methods</b>	<b>8</b>
<b>2.1.1 Materials for spectroscopies</b>	<b>8</b>
<b>2.1.2 Circular Dichroism<sup>o</sup></b>	<b>8</b>
<b>2.1.3 Attenuated Total Reflectance<sup>o</sup></b>	<b>12</b>
<b>2.1.4 Nuclear Magnetic Resonance<sup>o</sup></b>	<b>14</b>
<b>2.1.5 Proteins Cloning and Expression<sup>s</sup></b>	<b>16</b>
<b>2.1.6 Wild-type Proteins Purification</b>	<b>17</b>
<b>2.1.7 Electrophysiology</b>	<b>19</b>
<b>2.2 In-silico Methods</b>	<b>21</b>
<b>2.2.1 Channel structural study*</b>	<b>21</b>
<b>2.2.1.1 Models setup*</b>	<b>21</b>
<b>2.2.1.2 Passive Ions Diffusion*</b>	<b>23</b>
<b>2.2.1.3 Structural Analyses*</b>	<b>23</b>
<b>2.2.2 Peptide structural study<sup>o</sup></b>	<b>24</b>
<b>2.2.2.1 Bioinformatic tools<sup>o</sup></b>	<b>24</b>
<b>2.2.2.2 MD simulations<sup>o</sup></b>	<b>25</b>
<b>Chapter 3. Results</b>	<b>28</b>
<b>3.1 Structural study in-vitro of the N-terminal domains of hVDACs</b>	<b>28</b>
<b>3.1.1 Circular Dichroism Spectroscopy<sup>o</sup></b>	<b>28</b>
<b>3.1.2 Infrared Spectroscopy<sup>o</sup></b>	<b>29</b>
<b>3.1.3 Nuclear Magnetic Resonance Spectroscopy<sup>o</sup></b>	<b>32</b>
<b>3.1.4 Discussion<sup>o</sup> of the spectropic results</b>	<b>34</b>
<b>3.2 Structural study in-silico of the N-terminal domains of hVDACs</b>	<b>39</b>
<b>3.2.1 Bioinformatic Tools<sup>o‡</sup></b>	<b>39</b>
<b>3.2.2 Molecular Dynamics Simulations<sup>o‡</sup></b>	<b>40</b>
<b>3.2.3 Discussion<sup>o</sup> of the computational results</b>	<b>42</b>
<b>3.3 Biophysical characterization of human VDAC channels</b>	<b>43</b>
<b>3.3.1 General Aspects*</b>	<b>44</b>
<b>3.3.2 The N-terminal domain in the three isoforms*</b>	<b>46</b>
<b>3.3.3 Channel breathing motions*</b>	<b>51</b>
<b>3.3.4 Ions passive translocation*</b>	<b>56</b>
<b>3.3.5 Ions Preferential localization inside the lumen*</b>	<b>61</b>
<b>3.3.6 His-tag containing hVDACs</b>	<b>66</b>
<b>Chapter 4 Conclusions and Outlook</b>	<b>72</b>
<b>References</b>	<b>75</b>

**\* The content of these paragraphs is derived from the following published paper: G. F. Amodeo, M.A. Scorciapino, A. Messina, V. De Pinto, M. Ceccarelli (2014) PLoS ONE 9: e103879. My individual contribution to this paper is the analysis of the data and the setting up of the models. I participated in the composition of the manuscript.**

**° The content of these paragraphs is derived from the following published paper: C. Guardiani, M.A. Scorciapino, G.F. Amodeo, J. Grdadolnik, G. Pappalardo, V. De Pinto, M. Ceccarelli, M. Casu (2015) Biochemistry 54 (36) 5646-5656. My individual contribution in this paper was: performing the CD, ATR and NMR experiments as well as the analysis. I participated in the composition of the manuscript.**

**‡ Courtesy of Dr. Carlo Guardiani, Department of Physics, University of Cagliari, Italy, who performed the computational study of the N-termini of the three human VDAC isoforms.**

**§ Courtesy of Dr. Daniel Pletzer, University of British Columbia, who performed the cloning of the wild types human VDAC isoforms.**



## **Acknowledgments**

I would like to take the opportunity to thank the people who support me and my work during the past three years of my PhD.

First of all, my supervisors Prof. Mariano Casu and Prof. Dr Mathias Winterhalter for giving me the chance to work in their research teams and for all the learnings I got from them. I would like to thank Prof. Matteo Ceccarelli and Prof. Vito De Pinto for the financial support and for the motivation they gave me since my Master thesis. I would also like to thank Prof. Dr. Dr. Roland Benz for giving me the chance to learn directly from him and by making me work in his lab. I also thank Dr. Mariano Andrea Scorciapino and Dr. Giorgia Manzo for introducing me to the analysis of the spectroscopic and computational data. I would like to acknowledge all the people both in Cagliari and in Bremen who supported me, professionally and emotionally, during my PhD: in particular, Dr. Corrado Pani, Dr. Iván Barcena-Urribarri, Dr. Tatiana Kolesnikova, Dr. Daniel Pletzer, Dr. Jules Philippe, Lorraine Bénier, Dr. Marzia Fantauzzi, Dr. Carla Cannas, Dr. Andrea Ardu and Dr. Viola Aru and all of my lab mates. Finally, I would like to thank my parents, my brothers and the whole family for their support and love. The author thanks the support from MIUR through the project PRIN-2010CSJX4F 2012-2015 “Intracellular channels and pores: structural and functional studies provide new rules for engineering artificial channels”; the DAAD and the Erasmus Project for the scholarship assigned for the research stay abroad. The author acknowledge PRACE Preparatory Access Type A 2010PA1392 for awarding access to Curie/Hermit based in France/Germany and the technical support from CRAY to install NAMD2.9 on Hermit, Germany. The author thanks CINECA for CPU time allocation through the ISCRA-C project Met-FLUX 2013.

*Dedicated to the memory of my beloved grandfathers who raised me as their own child and that I would have loved to have still by my side*



## Chapter 1 Introduction

Mitochondria are eukaryotic, membrane-enclosed, 1-10  $\mu\text{m}$  sized organelles, described as “cellular power plants” as they are responsible for the production of adenosine triphosphate (ATP) and oxidative phosphorylation. Signal transduction (buffering and storage of intracellular calcium), control of cell cycle and cell growth, as well as programmed cell death (apoptosis) are other important homeostatic processes governed by mitochondria. It is not surprising therefore that, despite extensive research efforts at elucidating the still un-established pathophysiology of neurological disease, mitochondrial dysfunction is hypothesised to play a substantial role, with their consequent emergence in neuroscience research today.

For decades, the permeability properties of the mitochondria have been assumed to be dependent mainly on the inner membrane (IMM) since the outer membrane had been defined as “leaky”. This leaky membrane was able to allow the flux of small ions and metabolites with no sort of specific control <sup>1</sup>. However, this assumption was due to the impossibility of a proper extraction of mitochondria. The latter was achieved around the mid of the 70’s when Schein et al. observed that the permeability of the OMM was indeed related to the presence of porins <sup>2</sup>. The most abundant porins occurring in the OMM are the voltage dependent anion selective channels (VDACs). Even if they had been previously studied they were not very well characterized until they were isolated from rat liver by Colombini in 1983 <sup>3</sup>.

VDACs are a small family of conserved proteins located in the outer mitochondrial membrane <sup>4-6</sup>. They conduct ions, metabolites and small molecules, among which the energetic nucleotides ATP, ADP and NADH <sup>7</sup>.

Three different VDAC isoforms have been characterized in higher eukaryotes,

encoded by three separate nuclear genes<sup>6,8</sup>. VDAC1 is the most abundant isoform in most cells, being ten and hundred times more prevalent than VDAC2 and VDAC3, respectively. It is thus not surprising that VDAC1 is the isoform most extensively characterized. Functionally, VDAC1 is anion selective and exhibits a single-channel conductance of ~3.5-4.0 nS in 1 M KCl at an applied voltage between -20 mV and

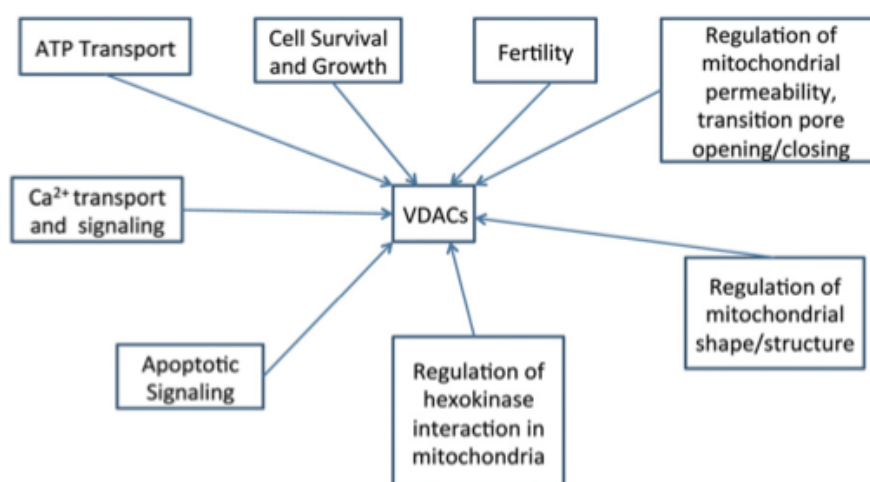


**Figure 1: VDACs functions** VDACs perform multiple functions: (1) regulating cell survival and cell growth, (2) fertility, (3) maintaining synaptic plasticity through MPT pore, (4) regulating calcium transport, (5) regulating ATP transport, (6) regulating mitochondrial shape and structural changes, (7) regulating hexokinase interactions with mitochondria and (8) regulating apoptosis signaling. Reprinted by permission from Elsevier (Reddy PH, *Biochim Biophys Acta* (2013) 1832: 67-75).

+10 mV<sup>4,5,9</sup>. Raising the applied voltage results in the channel switching to the so-called “closed state”, with a lower conductance and a channel selectivity reversed to cations<sup>7</sup>. In addition to the pore-forming function, VDAC1 has been involved in various interactions and cross-talk with other cellular proteins like hexokinase, tubulin, the Ca<sup>2+</sup> gate into mitochondria and the Bcl-2 family members that can impact on the activity of the pore itself and vice versa, testimony to the involvement of VDAC to crucial cell fates like in pathways leading to apoptosis, cancer and degeneration<sup>10-18</sup>.

After a long quest the structure of VDAC1 has been proposed by x-ray crystallography and nuclear magnetic resonance (NMR) methods to be a large

transmembrane channel (outer diameter  $\sim 4.5$  nm; inner diameter 2.0-2.5 nm; height  $\sim 4$  nm) formed by 19 amphipathic  $\beta$ -strands. Such an open barrel is made by the regular antiparallel organization of the  $\beta$ -strands, but the parallel pairing of the strands 1 and 19 completing the channel<sup>19-22</sup>. Whereas in bacterial porins an even number of antiparallel  $\beta$ -strands is generally observed, the structure of VDAC is absolutely peculiar<sup>23,24</sup>. It is not known whether this exception to the rule of an even number of

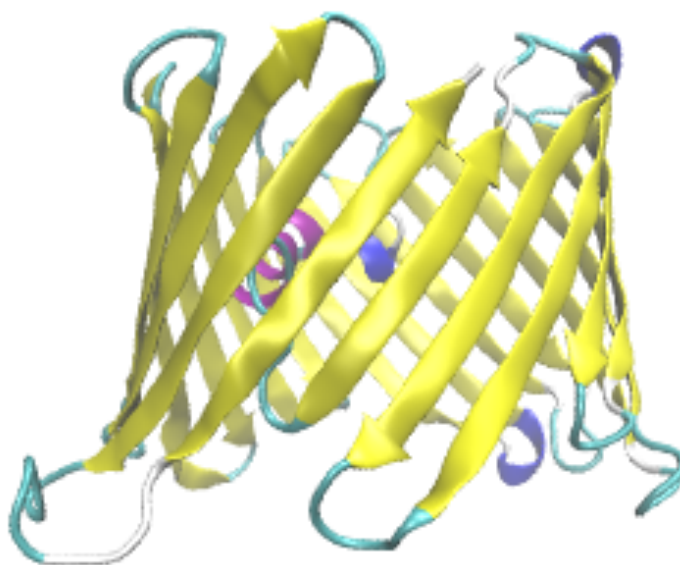


**Figure 2: 3D structure of hVDAC1.**

strands in protein  $\beta$ -barrels could have any influence on the stability and/or functionality of VDAC, and it has to be reported that several criticisms have been raised against this structure and whether it is the actual native conformation<sup>25</sup>. Conversely, a series of evidences have been reported in the literature to support the 19-strands structure against the previous models<sup>26,27</sup>. In addition, molecular dynamics simulations have shown that the X-ray/NMR solved structure is compatible with the experimental values of both conductance and ions selectivity of the open state<sup>28,29</sup>. The amino acid sequence of VDAC is highly conserved. The three human isoforms (hVDAC), in particular, are 68% to 75% pairwise identical, with 80-90% overall similarity. Figure 3 shows the sequence alignment of the three human isoforms of

VDAC. The high sequence homology among the hVDAC isoforms has been interpreted as a similarity among the respective 3D structures. The 3D structure of the VDAC2 and VDAC3 isoforms have been predicted on the basis of secondary structure prediction servers<sup>8</sup>. The most striking difference between the three human isoforms is certainly the longer N-terminal fragment of hVDAC2, which has 11 residues more than the other two isoforms (Fig. 1). The N-terminal fragment of VDAC, comprising the first 25 amino acid residues (36 in the case of hVDAC2), is located inside the channel in the 3D structure, partially closing the wide pore<sup>20-22</sup>. However, differences exist among the reported structures and they mainly refer about the N-terminus. This is due to a sum of factors like, for example, the temperature used in the NMR or in the crystallographic collection of experimental data. In human and mouse VDAC1, the N-terminal fragment crosses the lumen and is folded as an  $\alpha$ -helix from the residue 6 to 20, broken at the conserved residue G11<sup>20,22</sup>. This folded portion is actually amphipathic, with the more hydrophobic residues directed towards the barrel wall, while the hydrophilic ones point the lumen center. The same sequence has a mainly unfolded structure in the report by Hiller: it must be pointed out that the structure has been obtained with pure NMR, at room temperature<sup>21</sup>.

Because of these structural features, the N-terminal domain is considered to play a key role for both protein stability and functionality. It is crucial for the stabilization of the open state and in the voltage gating, as well as for the interaction with apoptosis related proteins<sup>6,17,26,28-35</sup>. hVDAC1 has no cysteines, whereas both hVDAC2 and hVDAC3 are characterized by the presence of two cysteines in the N-terminal region. It is not known whether they form disulfide bridges with other cysteines located in the barrel wall, but this should deeply affect the N-terminal mobility and, in turn, the specific isoform function. In the light of these differences and the different expression

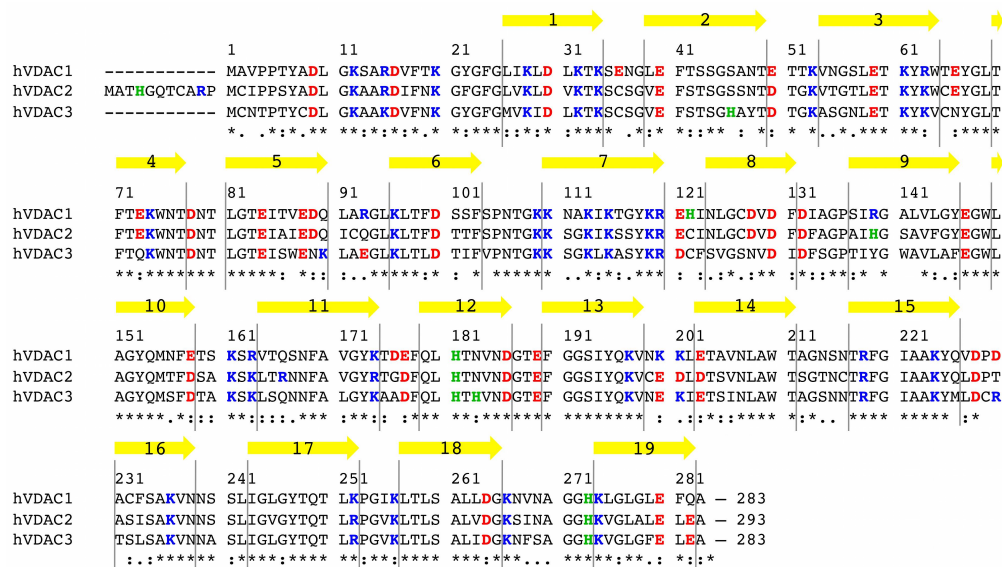


**Figure 3: Multiple sequence alignment of the three isoforms of hVDAC.** Residues are numbered according to hVDAC1 and hVDAC3 sequence (283 AA), thus, the first 11 N-terminal residues of hVDAC2 (293 AA) are not numbered in the figure and are referred to as 19-119 throughout the paper. Acidic residues are colored in red, basic ones in blue. Histidines have been distinguished from the latter and colored (green). The yellow arrows show the 19 b-strands forming the barrel. (Sequence alignment was obtained through ClustalW2 at <http://www.ebi.ac.uk/Tools/msa/clustalw2/>).

levels of the three human VDAC isoforms, the possibility of distinct and complementary roles has been put forward<sup>10,13</sup>.

### 1.1 Aim of the PhD thesis

The aim of the PhD project was to perform a comparative study on the human VDAC isoforms focusing on both the whole channels and the individuals N-terminal domains. In this sense, both experimental and computational techniques have been used pointing out their complementarity and contribute to the completeness of the study. These objectives may be summarized as follows:

1. Structural characterization of the N-terminal domains through both experimental and computational techniques;

2. Biophysical characterization of the human isoforms with the use of both electrophysiology and computational techniques such as molecular dynamics.



## Chapter 2 Methods

### 2.1 In-vitro methods

#### 2.1.1 Materials for spectroscopies

Synthetic peptides were purchased from Peptide Research Ltd. (Fareham, UK) with a purity of 98% and with the C-terminus amidated. In particular, (1-25)hVDAC1 [MAVPPTYADLGKSARDVFTKGYGFG], (12-36)hVDAC2 [MCIPPSYADLGKAARDIFNKGFGFG] and (1-25)hVDAC3 [MCNTPTYCDLGKAAKDVFNKGYGFG] were investigated. The 3-(trimethylsilyl)-2,2',3,3'-tetra-deuteriopropionic acid (TSP) was purchased from Cambridge Isotope Laboratories (Andover, MA, USA). All other chemicals were supplied by Sigma-Aldrich. Peptides were dissolved in 10 mM phosphate buffer (PB; pH=7.4) at a final concentration dependent upon the specific investigation technique employed. In the case of (12-36)hVDAC2 and (1-25)hVDAC3, due to the occurrence of cysteines in the amino acid sequence, the reducing agent DL-Dithiothreitol (DTT) was added at a 1:3 peptide/DTT ratio in order to avoid the formation of disulfide bridges.

#### 2.1.2 Circular Dichroism (CD)

Plane polarised light can be split into two vector components of equal magnitude rotating clockwise (left-handed) and counter-clockwise (right-handed) respectively. The term Circular Dichroism (CD) refers to the different absorption of an optically

active (i.e. chiral) molecule of these two components. The absorption of either one or the other component by a chromophore leads to the loss of the phase of the two vectors that will rotate at different speeds describing an elliptical curve as shown in Figure 4.

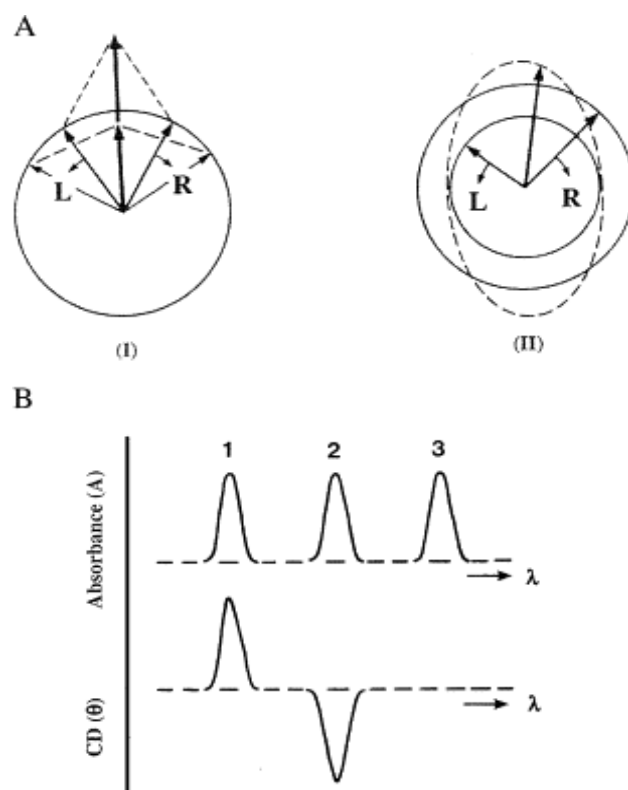


**Figure 4: Origin of the CD effect.** (A) The left (L) and right (R) circularly polarised components of plane polarised radiation: (I) the two components have the same amplitude and when combined generate plane polarised radiation; (II) the components are of different magnitude and the resultant (dashed line) is elliptically polarised. (B) The relationship between absorption and CD spectra. Band 1 has a positive CD spectrum with L absorbed more than R; band 2 has a negative CD spectrum with R absorbed more than L; band 3 is due to an achiral chromophore. Reprinted by permission from Elsevier Kelly SM et al. *Biochim Biophys Acta* (2005) 1751 (2): 119-139.

This spectroscopic technique has been widely used since the interest in structure biology raised exponentially in the 80's. Indeed, most of the biomolecules are either optically active or occur in an asymmetrical environment. Indeed, most of the biomolecules are either optically active or occur in an asymmetrical environment. The

former is given by the occurrence of one or more chiral groups, whereas the latter is mainly due by the 3D conformations of biomolecules. Nowadays, the main applications of this technique rely on the study of the secondary and tertiary structure of proteins or on the effects of the chelation of DNA complexes.

In the case of proteins, different chromophore groups occur at the same time:

- the peptide bond, whose absorption is within the ultraviolet spectral range (i.e. 190 nm up to 260 nm);
- the aromatic side chains of aa, i.e tyrosine, tryptophan and phenylalanine;
- the disulphide bridges, weakly absorbing around 260 nm.

The vicinity of these chromophores within a protein leads them to act as an exciton, i.e. a whole absorbing unit resulting in a specific spectral shape according to their geometry.

The main information that can be obtained from CD studies of protein is the estimation of the secondary structure composition. This can be done by observing the spectral shape of the sample in the absorption region of the peptide bond. When irradiated within the ultraviolet wavelengths, the following electronic transitions of the peptide bond take place:

- $n \rightarrow \pi^*$  at 220 nm (weak and broad)
- $\pi \rightarrow \pi^*$  at 190 nm (intense and narrow)

According to the secondary structure of the sample, these bands will be modified resulting in the characteristic spectra shown in Figure 5.

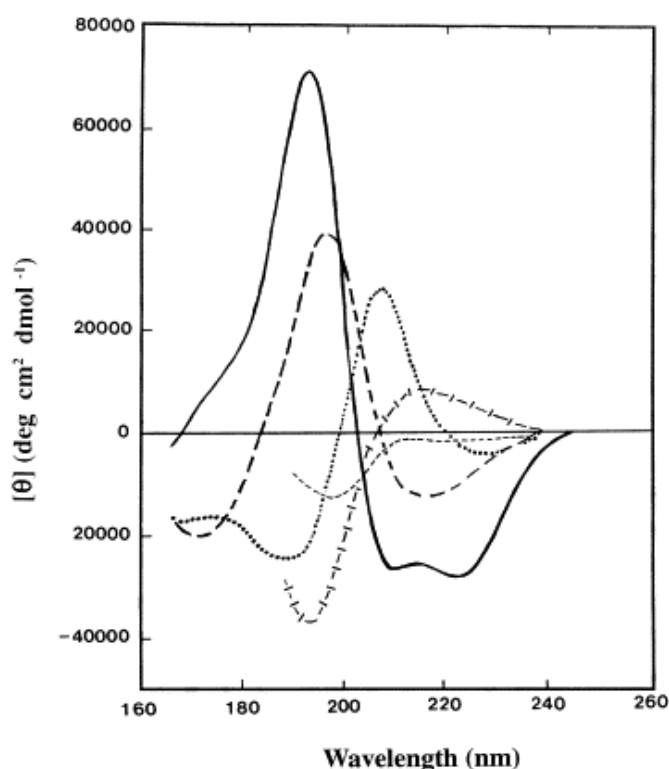


**Figure 5: Far UV CD spectra associated with various types of secondary structure.** Solid line,  $\alpha$ -helix; long dashed line, anti-parallel  $\beta$ -sheet; dotted line, type I  $\beta$ -turn; cross dashed line, extended  $3_1$ -helix or poly (Pro) II helix; short dashed line, irregular structure. Reprinted by permission from Elsevier Kelly SM et al. *Biochim Biophys Acta* (2005) 1751 (2): 119-139

CD spectra of the three peptides (20  $\mu$ M) were recorded on a Jasco J-810 spectropolarimeter with a 1-mm path length cell. Spectra were recorded in the 190-260 nm spectral range, with a scan rate of 10 nm/min at 0.1 nm intervals. Data acquisition was performed at 300 K and averaging 10 scans for each spectrum. Peptides CD spectra were collected either in 10 mM PB and in the presence of additional electrolytes to investigate the effect of physiologically relevant counterions on the peptide intrinsic folding propensity. In particular, either  $\text{Na}^+$  or  $\text{K}^+$  ions were added to the PB at a final concentration of 100 mM, in order to test the effect of a large excess of these monovalent cations, matching a typical physiological condition.

Also the presence of  $Mg^{2+}$  ions was checked but keeping the Mg/peptide molar ratio to 1/1. Cations were added to the PB as dibasic sulphate salts. Despite chlorides are more physiologically relevant anions, they strongly absorb below 195 nm and are therefore not recommended for CD investigations <sup>36</sup>.

### 2.1.3 Attenuated Total Reflectance (ATR-FTIR)

Fourier transform infrared spectroscopy is acknowledged among the standard techniques used to determine the structure of small molecules. The sensitivity of this technique make it feasible for the study of protein samples whose spectra can give a huge amount of information on the structure. The infrared radiation excites the vibrational modes of the molecules. In the case of the protein study, the interest is mainly focused on the bands given by the vibrations of the peptide bond and the backbone residues. The stretching mode of the carbonyl group within the former gives rise to the Amide I band ( $1700-1600\text{ cm}^{-1}$ ) whose shape and wavelength will be due to the sum of the different secondary structure components. Moreover, other bands occur in the IR spectrum of a protein sample, namely, amide A, B and II-VII. Amide II and III, as well as amide I, result from other vibrational modes of the peptide bond and are less intense. Hence, they are less relevant in terms of information than the amide I band. The remaining protein bands are more complex and derive mainly from the side chains of the aa and hydrogen bonds.

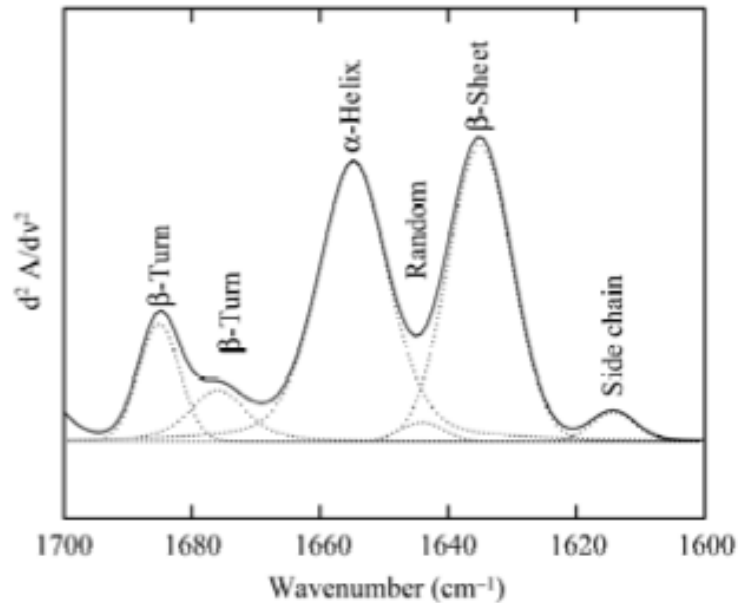


**Figure 6: Second derivative infrared spectrum of cAMP receptor protein in Tris buffer.** Curve-fitted second derivative spectrum was carried out by factoring-1. The curve fitting was carried out by BOMEM GRAMS/32 software. Reprinted by permission from Oxford University Press, Kong J et al. *Acta Biochim Biophys Sinica* (2007) 1751 (2): 119-139

Among the different IR technique, the attenuated total reflectance (ATR) is one of the most sensitive. It requires a very small amount of sample and it suitable for measure the sample without any pre-treatment. In fact, a drop of the protein sample is placed on a crystal surface and the reflected radiation is then detected, as shown in Figure 7. The crystal possesses a larger refraction index compared to the sample, so that the radiation, directed at a certain angle is totally reflected. After variable reflections, light penetrates the sample and decays proportionally with the distance from the interface creating an evanescent wave. This wave can be absorbed buy the sample resulting in an infrared spectrum.

Spectra were recorded on liquid-state samples (10  $\mu\text{L}$ ) at room temperature with a Bruker Vector 22 spectrometer equipped with a diamond single reflection ATR accessory (Platinum ATR module) and a liquid- $\text{N}_2$  cooled MCT-detector. Spectra were acquired in the  $4000\text{-}600\text{ cm}^{-1}$  range ( $4\text{ cm}^{-1}$  spectral resolution) and averaging 256 scans. Peptide concentration was 7 mM. For each sample, water evaporation was

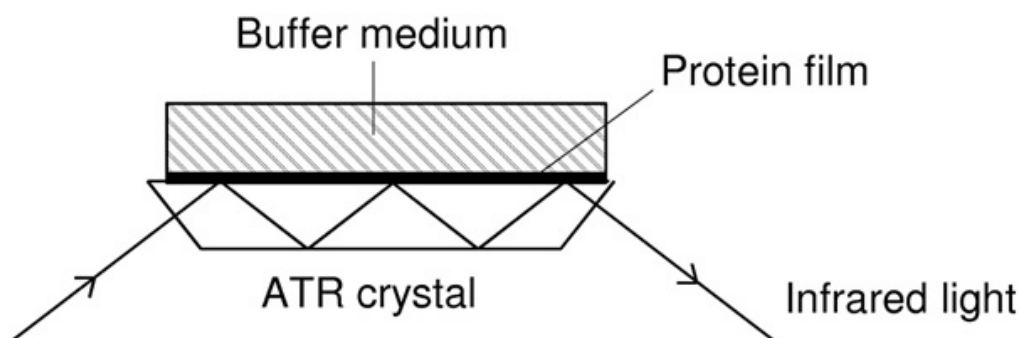


**Figure 7: A typical ATR setup.** Reprinted by permission from Elsevier Barth A Biochim Biophys Acta (2007) 1767 (9): 1073-1101.

followed; in addition, by recording a spectrum every 5 minutes until no further spectral changes were observed. On average, 40 minutes were necessary to get almost complete water evaporation and obtain a spectrum of the solid film formed on the surface of the diamond. The formation of the solid film significantly improved signal/noise ratio and band resolution. ATR-IR spectra of peptides were collected in 10 mM PB and in the presence of additional electrolytes. In particular, Na<sup>+</sup>, K<sup>+</sup> or Mg<sup>2+</sup> ions were added at a final concentration of 100, 100 or 7 mM, respectively. Cations were added to the PB as chloride salts.

#### 2.1.4 Nuclear Magnetic Resonance (NMR)

Since the first resolution of a protein structure in 1984 by Wüthrich, NMR has become one of the most powerful techniques to investigate the three-dimensional conformation of biomolecules<sup>37</sup>. Whilst, CD and ATR give an estimation of the secondary structure, NMR can give information at the atomic level. In fact, by using a set of one- and two-dimensional experiments it is possible to obtain the geometrical parameters of the sample conformation from the spectral data. The main spectral parameters correlated to proteins are the following:

- Chemical shifts;

- Coupling constants;
- Dipolar interactions.

The values of the chemical shift of a given protein sample can be compared with the values of the chemical shift index (CSI). It is a method based on the fact that a specific secondary structure causes the shift either to upfields (helices) or downfields (beta strands). Hence, the comparison between the experimental values and the random coil gives a first estimation of the secondary structure.

The coupling constants gives information about the nearby environment of an atom. In particular, the experimental values of the vicinal coupling constants can be used in the Karplus equation determining the dihedral angle among three atoms.

Dipolar interactions can be detected thank to nuclear Overhauser effect (NOE) according to which the magnetization is transferred among non-bonded atoms. The detection of the cross-peaks in a NOESY experiment will give information about the long-range interaction within the sample that will be strongly dependent on the 3D structure.

Peptides were dissolved in PB at a concentration of 2 mM. The pH was corrected to 5.0 with small aliquots of 0.1 M HCl in order to minimize backbone amide protons exchange rate with water<sup>38</sup>. Spectra were acquired with a Agilent Unity Inova 500NB operating at a <sup>1</sup>H frequency of 500 MHz. Experiments were carried out at 300 K. The chemical shift scale of both <sup>1</sup>H and <sup>13</sup>C was referenced to the methyl signal of TSP (2 mM). <sup>1</sup>H spectra were acquired using a 6.6 μs pulse (90°), 1 s delay time, 2 s acquisition time and a spectral width of 7 kHz. Suppression of the water signal was achieved through the application of the WET sequence (uburp shape was centered at water resonance with a width of 100 Hz)<sup>39,40</sup>. <sup>1</sup>H-<sup>1</sup>H DQF-COSY experiments were recorded over the same spectral window using 2048 complex points and sampling

each of the 512 increments with 64 scans. The same acquisition parameters have been applied, together with a mixing time of 80 ms (MLEV-17 spin-lock scheme), for the acquisition of TOCSY spectra. The NOESY experiments were run with the same acquisition parameters and a mixing time of either 200 and 250 ms. The  $^1\text{H}$ - $^{13}\text{C}$  HSQC spectra were collected using a spectral window of 7 and 21 kHz for  $^1\text{H}$  and  $^{13}\text{C}$  respectively, and sampling each of the 512 increments with 64 scans. The  $^3\text{J}_{\text{HNH}\alpha}$  coupling constants were measured from DQF-COSY spectra. The chemical shift values of  $^1\text{H}_\alpha$ ,  $^1\text{H}_\beta$ ,  $^{13}\text{C}_\alpha$  and  $^{13}\text{C}_\beta$  were analyzed through the software TALOS+ in comparison to its high-resolution structural database <sup>41</sup>.

#### 2.1.5 Proteins cloning and expression

hVDAC genes containing a 6xHis fused to the C-termini (N-terminus for hVDAC2) were cloned into the pET21a vector (Novagen) using NdeI/XhoI sites. Escherichia coli BL21 Rosetta strain cells were transformed with pET21a harboring the hVDAC genes. Transformants were grown in LB medium containing ampicillin ( $100\ \mu\text{g}/\text{ml}^{-1}$ ). Induction was performed by addition of 1 mM isopropyl- $\beta$ -D-thiogalactopyranoside (IPTG) at an optical density ( $\lambda = 595\ \text{nm}$ ) of  $\sim 0.6$ . Proteins were purified in urea by chromatography using nickel-nitrilotriacetic acid resin (Ni-NTA, Qiagen). The denatured protein mixture was added drop-wise to 25 mM TrisHCl (pH 7.0), 100 mM NaCl, 1 mM EDTA, 1% (v/v) lauryldimethylamine-oxide (LDAO), allowing a ten-fold dilution of the urea concentration, and the mixture was gently stirred overnight at  $4^\circ\text{C}$ . The protein solution was then dialyzed against a 100x buffer containing 0.1% LDAO overnight at  $4^\circ\text{C}$ . Thermo Scientific Slide-A-Lyzer Dialysis Cassettes (3.5 K MWCO) were used to avoid any sample loss. The protein purity was verified by 12%

SDS-PAGE and Silver staining. Purified samples were stored at 4°C until further use. In order to express hVDAC1 and hVDAC3, respectively, without a tag, the genes were cloned into pET16b via NcoI/BamHI. For hVDAC3 an additional Glycine was added to be in-frame. hVDAC2 was amplified from a yeast shuttle vector pYX212 using primer pairs as indicated below. Expression without a tag was achieved by cloning the gene via XbaI/XhoI in pET16b. All obtained constructs were sequenced and subsequently transformed into BL21/Rosetta2 strains, carrying plasmid pRARE2 (encoding tRNAs for rarely used codons in *E. coli*: AUA, AGG, AGA, CUA, CCC, GGA, and CGG) to enhance expression of eukaryotic proteins. Protein expression was prepared by an overnight culture of a single colony in dYT medium containing 100 µg/mL of ampicillin and 25 µg/mL of chloramphenicol. Next, the overnight culture was diluted to an OD<sub>600</sub> of 0.01 in 50 mL dYT medium and grown until they reached an OD<sub>600</sub> of 0.6. Induction of gene expression was done by adding 1 mM IPTG for 3 hours at 37 °C. Cells were then harvested by centrifugation at 4000 rpm for 20'. The resulting pellet was prepared for protein extraction from inclusion bodies by overnight incubation in 20 mL 8 M urea (phosphate buffer, pH 8.0). The next day, the suspension was ultra centrifuged for 30' at 13,000g. The obtained crude extracts were ran on 10% SDS-PAGE for proper overexpression. The cleared lysate was subsequently stored at -20 °C.

#### 2.1.6 Wild-type Protein Purification

Ion exchange chromatography involves the separation of ionizable molecules based on their total charge. It is commonly used to separate charged biological molecules such as proteins, peptides, amino acids, or nucleotides.

The amino acids that make up proteins are zwitterionic compounds that contain both positively and negatively charged chemical groups. Depending on the pH of their environment, proteins may carry a net positive charge, a net negative charge, or no charge. The pI value (i.e. the pH at which a molecule has no net charge) can be calculated based on the primary sequence of the molecule. The choice of buffer pH then determines the net charge of the protein of interest. In a buffer with a pH greater than the pI of the protein of interest, the protein will carry a net negative charge; therefore, a positively charged anion exchange resin is chosen to capture this protein. In a buffer with a pH lower than the pI of the protein of interest, the protein will carry a positive net charge; thus a negatively charged cation exchange resin is chosen. When an ion exchange chromatography column is loaded with a sample at a particular pH, all proteins that are appropriately charged will bind to the resin. After loading an impure protein sample onto an ion exchange chromatography column, the column is washed to remove undesired proteins and other impurities, and then the protein(s) of interest is eluted using either a salt gradient or a change in pH. In the former case, the charged salt ions compete with bound proteins for the charged resin functional groups. Proteins with few charged groups will elute at low salt concentrations, whereas proteins with many charged groups will have greater retention times and elute at high salt concentrations. In the latter case, a pH gradient is chosen that approaches the protein of interest's pI. Proteins will elute when the pH gradient reaches their pI, because they will no longer carry a net charge that allows them to interact with the column resin.

Fast protein liquid chromatography (FPLC) is a form of medium-pressure chromatography that uses a pump to control the speed at which the mobile phase passes through the stationary phase. FPLC was introduced in 1982 by Pharmacia as fast performance liquid chromatography. Fast protein liquid chromatography systems generally consist of a pump, a UV detector, a conductivity meter, and a fraction collector and operate at pressures of ~3,500 psi (24 MPa).

1 mL Aliquots of the cleared lysate were used for purification via FPLC using the MonoQ anion affinity column (GE Healthcare). pH 8 was used for the mobile phase buffer. The protein sample was injected onto the column after filtration with 0.22  $\mu\text{m}$  filters. A gradient of linearly increasing salt concentration is then applied to elute the sample components from the column. The buffers used for the chromatography, namely buffer A and B, were both composed of 20 mM TrisHCl and 1% LDAO. Buffer B also contained 1 M NaCl in order to increase the salt gradient. Fractions were tested on 10% SDS-PAGE and the ones showing the pure protein were subsequently used for the electrophysiological characterization.

### 2.1.7 *Electrophysiology*

Lipid membranes present an excellent insulator for small ions. Due to their high electrical resistance any ion-conducting channel reconstituted into such an insulator will increase the conductance.

The pore forming activity of the purified proteins was verified by the use of black lipid bilayer (BLB) assay<sup>42</sup>. The membranes were formed from a 1% (w/v) solution of DPhPC 1,2-diphytanoyl-sn-glycero-3-phosphocholine (DPhPC), (Avanti Polar Lipids, Alabaster, AL) in n-decane. The membranes had a surface of

approximately  $0.5 \text{ mm}^2$  and they were formed using a Teflon loop to spread the lipid over the aperture. The porin-containing protein fractions were diluted to 1:1 ratio in 1% Genapol (Roth) and added to the aqueous phase after the membrane had turned black. The membrane current was measured with a pair of reference Ag/AgCl electrodes with salt bridges switched in series with a voltage source and a highly sensitive current amplifier (Keithley 427). The signal was recorded by an analog strip chart recorder (Rikandenki).

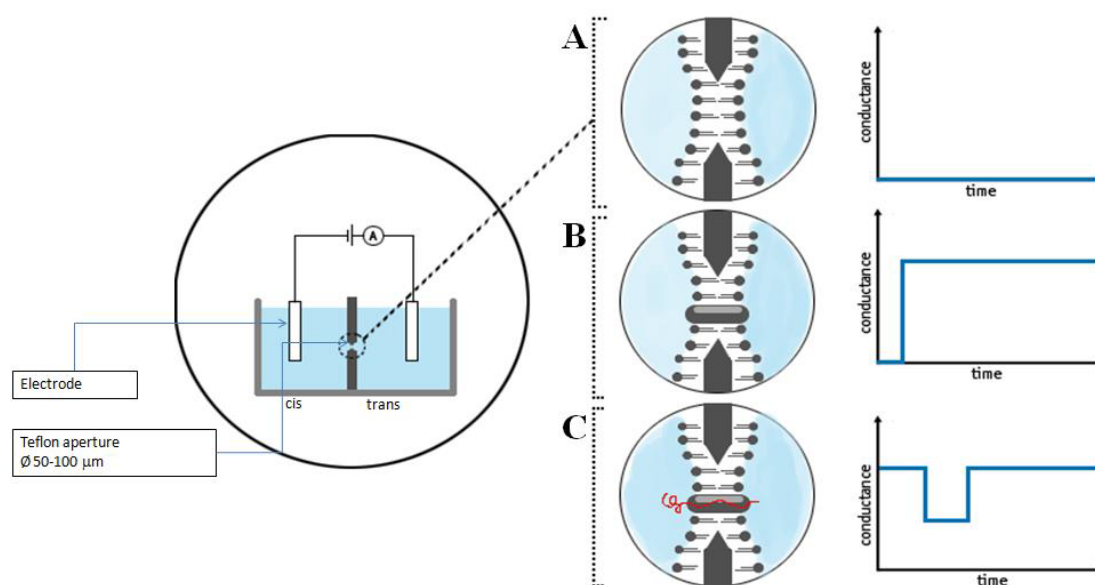


**Figure 8: Experimental Setup of a planar lipid bilayer set up.** A) a electrically insulating bilayer, B) the jump in conductance over time with the insertion of a single protein channel in the lipid bilayer, and C) the interaction of a substrate (in red) with the protein channel, observed by the drop in conductance due to the blockage of ion current through the pore for a certain period of time, which is the time of residence of the substrate in the pore. Reprinted from Usha Lamichhane PhD proposal.

Single channel measurements were performed following the monolayer technique of Montal and Müller<sup>43</sup>. The bilayer is formed by two monolayers juxtaposed and extended across a hole that is  $\approx 100 \text{ }\mu\text{m}$  in diameter in a  $25 \text{ }\mu\text{m}$  thick polytetrafluoroethylene (PTFE) film. Prior to bilayer membrane formation, the aperture is pre-painted with  $1 \text{ }\mu\text{L}$  of a 1% v/v solution of n-hexadecane in n-hexane to make it lipophilic. After being dried for 10 min, both chambers are filled with buffer, i.e. 1 M KCl and either 10 mM of HEPES (pH 7.2) for the His-tagged proteins or 20

mM MES (pH 5.5) for wild-type proteins, and a lipid bilayer is prepared by spreading 2.5  $\mu$ L of a 5 mg/mL solution of DPhPC in a solvent mixture of n-pentane in the aperture. Ag/AgCl electrodes are used to detect the ionic currents. The electrode on the cis side of the cell is grounded, whereas the other one on the trans side is connected to the headstage of an Axopatch 200B amplifier. Purified detergent-solubilized porins (both the stock and the 1:1 dilution in 1% Genapol) are added to the cis side of the chamber and inserted into the bilayer membrane in absence of voltage.

## **2.2 In-silico methods**

### *2.2.1 Channels structural study*

#### *2.2.1.1 Models setup*

The experimental structure of mVDAC1 obtained with X-ray crystallography was used as the starting configuration (PDB code 3EMN at 2.3  $\text{\AA}$  resolution)<sup>22</sup>. The three hVDAC isoforms were built by homology modeling using the Modeller v9.10 software<sup>44,45</sup>.

The protein was embedded in a pre-equilibrated POPE hydrated bilayer. (i) Lipids were eliminated to create a pore with a radius of 2 nm, (ii) the protein was inserted, (iii) the system was oriented in order to center protein at the origin of the coordinate system and align the channel with respect to the z-axis, (iv) additional lipid molecules at a distance  $< 2 \text{\AA}$  from the protein were removed. A suitable number of chloride ions were added in order to neutralize system total charge. The edges of the simulation box were initially 82x82x95  $\text{\AA}$ , with  $\sim 170$  lipids and  $\sim 10000$  water molecules (total

number of atoms  $\sim 56000$ ). Both the N- and the C- protein termini were located on the positive-z side of the bilayer.

After 1 ps of energy minimization to remove bad contacts, a slow heating from 10 to 300 K was carried out for 1 ns. During this stage, positional restraints were applied on the protein alpha-carbons (all three dimensions) as well as on the lipids phosphorus atoms (along z only). Then, an equilibration stage follows for 10 ns in the NPT ensemble at 1.0 bar and 300 K allowing for waters and lipids rearrangement and box equilibration. Finally, 1.0  $\mu$ s MD simulations were performed in the NVT ensemble by using the box size reached during the NPT equilibration stage (81.58x81.58x84.25 Å for hVDAC1, 81.86x81.86x83.09 for hVDAC2 and 81.86x81.86x83.03 for hVDAC3). The first 200 ns were considered part of the equilibration stage, while the last 800 ns were used for the analyses.

The NPT equilibration MD simulations were performed with the program NAMD, with 1.0 fs time-step, and treating long-range electrostatics with the Soft Particle Mesh Ewald (SPME) method (64 grid points and order 4 with direct cutoff at 1.0 nm and 1.0 Å grid-size)<sup>46</sup>. Pressure control was applied using the Nose-Hoover method (extended Lagrangian) with isotropic cell, integrated with the Langevin Dynamics (200 fs and 100 fs of piston period and decay, respectively). The latter was also applied for temperature control with 200 fs thermostat damping time.

Production runs in the NVT ensemble were performed through the ACEMD code compiled for GPUs<sup>47</sup>. The code allowed to rescale hydrogen mass to 4 amu and to increase the time-step up to 4.0 fs. The Langevin thermostat was used with 1 ps damping coefficient. SPME was used to treat electrostatics as done during the equilibration stage. Simulations were restarted every 200 ns with new randomly generated velocities. Random numbers generator seed was also changed every restart

in order to introduce additional noise and achieve better sampling of the conformational space. This procedure should prevent the system from being trapped in a single potential basin <sup>48</sup>.

All MD simulations were performed employing the Amber99SB-ILDN force field for the protein and lipids, and the TIP3P for waters <sup>49,50</sup>.

#### 2.2.1.2 *Passive Ions Diffusion*

Additional production runs were performed for each hVDAC isoforms in the presence of 0.5 M KCl. The starting coordinates were taken from the frame corresponding to 200 ns of the above-mentioned NVT simulations. Using the same parameters reported hereinbefore, we re-equilibrated the system (after KCl addition) in the NPT ensemble for 2 ns and then we moved to the NVT ensemble for 200 ns. Starting from the last configuration, we performed 5 independent 100 ns long MD replicas with different initial velocities.

#### 2.2.1.3 *Structural Analyses*

Channel radius was calculated for each 0.5 Å section normal to the z-axis from the solvent accessible area, using a probe with a radius of 1.4 Å <sup>51</sup>. Residues hydrophobicity scores were obtained with the method of Kyte and Doolittle using a window of 3 residues and a relative weight of the window edges of 30% when compared with the window center <sup>52</sup>. Hydrogen bonds, secondary structure analysis and correlation maps were obtained with the Simulaid package <sup>53</sup>. Protein electrostatic

potential surfaces were computed with the Adaptive Poisson-Boltzmann Solver (APBS) tool within the Visual Molecular Dynamics (VMD) software<sup>54-58</sup>.

Free-energy profiles for chloride and potassium ions were calculated according to the following equation<sup>59</sup>:

$$(1) \quad \Delta G_i(z) = -k_B T \ln \left( \frac{\rho_i(z)}{\rho_{bulk}} \right)$$

where  $\Delta G(z)$  is the free-energy as function of the  $z$ -coordinate,  $k_B$  is the Boltzmann constant,  $\rho_i(z)$  the ions density as functions of the  $z$ -coordinate and  $\rho_{bulk}$  is the averaged ions density outside the pore.

In order to investigate preferential localization of oppositely charged ions in the hVDAC lumen, a cluster analysis was applied to the coordinates of chloride and potassium ions along the MD simulations ( $-20 \leq x,y,z \leq 20$ ), with a rmsd of 6.0 Å and minimum occurrence of 10%. Basically, the positions recorded along the entire trajectory for all the ions of the same type are used. The number of neighbors within the given rmsd value are counted for each position. The position with the highest number of neighbors is taken together with its neighbors to define the most populated cluster. All the positions assigned to the first cluster are then eliminated from data pool and the procedure is iteratively repeated to look for the other clusters.

## 2.2.2 Peptide structural study

### 2.2.2.1 Bioinformatic tools

Polarity score for amino acids was calculated through the ExPASy web portal, available on the Internet at <http://expasy.org/>. The method of Grantham has been applied over windows of 3 residues and rescaling by 50% the score of the window edges<sup>60</sup>. Helical propensity was estimated with the predictive algorithm Agadir at a temperature of 300K, ionic strength of 0.1 M and pH 7.4<sup>61-63</sup>.

#### 2.2.2.2 *MD simulations*

Simulations started with the peptide in the fully extended conformation, embedded in a truncated octahedral simulation box comprising ~10000 water molecules. Sodium and chloride ions have been added to the systems to neutralize the peptide net charge and reach a final NaCl concentration of 10 mM. All simulations were performed with Amber14 using the ff14SB force field and the TIP3P water model. In order to avoid possible entrapment in metastable minima, the enhanced sampling technique Hamiltonian Replica Exchange MD (H-REMD) was employed<sup>64-66</sup>. Differently than canonical REMD, all replicas were run at the same temperature and exchanges were attempted between replicas on the basis of the torsional energy or the backbone dihedral angles<sup>67</sup>. The dihedral force constants were all uniformly scaled by a constant factor, from 1.0 (full force field) to 0.3 in intervals of 0.1, leading to eight replicas<sup>68</sup>. Each replica first underwent 1000 steps of steepest descent minimization followed by 1000 steps of conjugate gradient minimization. Replicas were then equilibrated for 5 ns in the NVT ensemble using a time-step of 2 fs and a temperature of 300 K with the Langevin thermostat. The last frame was used as input for the subsequent H-REMD simulation. Each replica was run for 100 ns attempting exchanges every 2.5 ps (acceptance probability in the range 55-65%).

The secondary structure analysis of the trajectory with full torsional force ( $\lambda=1.0$ ) was performed using the DSSP algorithm<sup>69</sup>. CD spectra were calculated on the basis of the MD trajectories as a linear combination of experimental reference spectra for purely  $\alpha$ -helix,  $\beta$ -sheet and random-coil conformation, where the weighting factors are the frequencies obtained from the DSSP analysis<sup>70,71</sup>.



## Chapter 3 Results

Here in this chapter we summarize the results. First we focus on the determination of the structure of the N-termini of human VDAC isoforms using spectroscopy determining the existence of an equilibrium among different secondary structures. A second set of data obtained with computational techniques and bioinformatics tools will be presenting supporting the experimental results. In a following section, the focus will be shifted to the characterization of the entire protein. First, the results obtained from the conformational study with MD will be reported, starting from analysis of the N-termini within the whole channel. Subsequently, the electrostatics and the analysis of the ion diffusion will be presented. Finally, the electrophysiological study on the three channels will be treated.

### 3.1 Structural characterization in-vitro of the N-terminal domains of hVDACs

#### 3.1.1 Circular dichroism spectroscopy

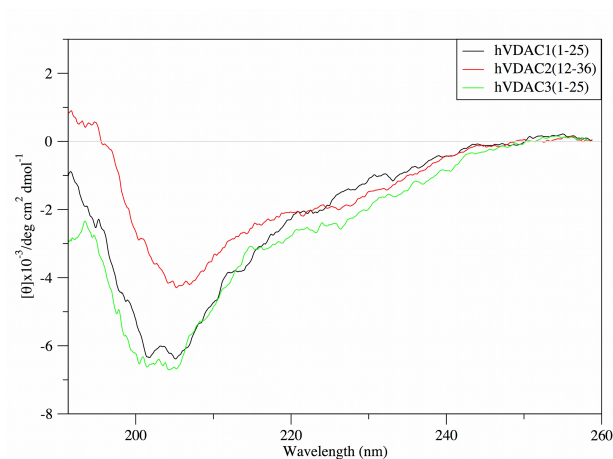


**Figure 9: CD spectra of hVDACs N-terminal peptides.** Spectra acquired in phosphate buffer (10 mM; pH 7.4) are shown with the ordinate reporting the mean residue ellipticity.

The CD spectra obtained for the three peptides in PB are shown in Figure 9. Spectra of hVDAC1(1-25) and hVDAC3(1-25) show a similar spectral shape, with a main broad negative band at a wavelength slightly higher than 200 nm, and negative ellipticity in the 190-195 nm range. On the other hand, the spectrum of hVDAC2(12-36) is remarkably different. The main negative band is characterized by a lower ellipticity and is shifted towards a higher wavelength, while slightly positive ellipticity is observed in the 190-195 nm range. Moreover, the presence of at least one additional negative band around 220 nm is evident in this case. Actually, the presence of a similar additional band for the other two peptides cannot be ruled out.

The influence of different cations, namely  $\text{Na}^+$ ,  $\text{K}^+$  and  $\text{Mg}^{2+}$ , was also investigated. Figure 10 shows the CD spectra acquired on the three peptides in the presence of the different metal ions added to the PB. No dramatic differences were observed in the spectral shape or in the bands position, indicating that, in our experimental conditions, the influence of such cations on the conformational equilibrium was negligible for each of the three peptides under investigation. However, in the presence of 1 equivalent of  $\text{Mg}^{2+}$ , the spectrum of both hVDAC1(1-25) and hVDAC3(1-25) resulted to be similar to those obtained for the hVDAC2(12-36).

### 3.1.2 *Infrared spectroscopy*

IR spectra were recorded in the ATR mode on both the liquid-state samples and the corresponding solid film. The latter were always characterized by a significantly higher S/N ratio and band resolution. In addition, spectrum background subtraction was easier and more effective for the films, and fewer artifacts were introduced when compared to the liquid-state spectra.

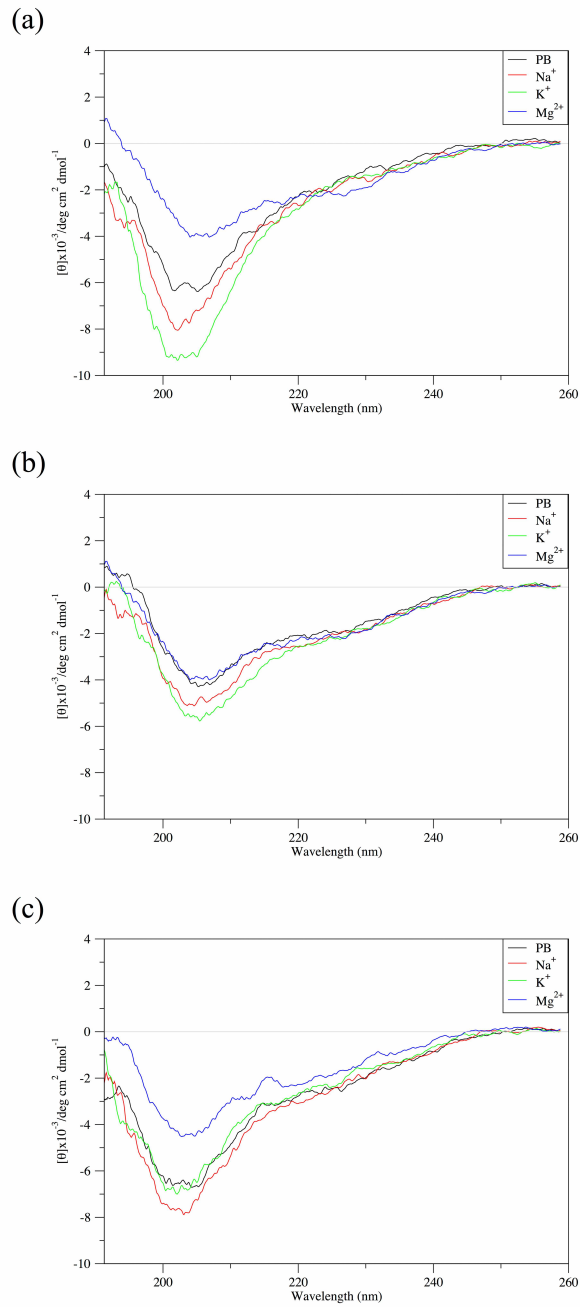


**Figure 10: Cations effect on CD spectra of hVDACs N-terminal peptides.** Spectra acquired in the presence of  $\text{Na}^+$ ,  $\text{K}^+$  or  $\text{Mg}^{2+}$  in the phosphate buffer (10 mM pH 7.4). The spectrum obtained in the buffer (Fig.9) is also shown for direct comparison.

The position of the maximum of the amide I band was measured for each of the three investigated peptides, either in the absence and presence of different cations in the PB, namely  $\text{Na}^+$ ,  $\text{K}^+$  and  $\text{Mg}^{2+}$ . The full width at half maximum (FWHM) was also

estimated by fitting the amide I band with a single Gaussian function. No band deconvolution was attempted to quantify different components. Table 1 reports the results.

**Table 1. Infrared amide I band position and width for the N-terminal peptide of hVDACs (7 mM) in the absence and presence of different cations in the phosphate buffer (spectral resolution 4 cm<sup>-1</sup>).**

	Wavenumber (FWHM) [cm <sup>-1</sup> ]			
<b>film-spectra</b>	<sup>a</sup> PB	<sup>b</sup> Na <sup>+</sup>	<sup>b</sup> K <sup>+</sup>	<sup>c</sup> Mg <sup>2+</sup>
hVDAC1(1-25)	1648 (61)	1648 (60)	1648 (62)	1648 (61)
hVDAC2(12-36)	1653 (52)	1653 (53)	1654 (52)	1654 (50)
hVDAC3(1-25)	1653 (52)	1656 (48)	1650 (52)	1654 (51)
<b>liquid-spectra</b>	<sup>a</sup> PB	<sup>b</sup> Na <sup>+</sup>	<sup>b</sup> K <sup>+</sup>	<sup>c</sup> Mg <sup>2+</sup>
hVDAC1(1-25)	1644 (63)	1642 (76)	1642 (82)	1644 (69)
hVDAC2(12-36)	1646 (71)	1639 (77)	1647 (71)	1649 (59)
hVDAC3(1-25)	1652 (87)	<sup>d</sup> ---- (--)	1648 (60)	1649 (55)

<sup>a</sup> 10 mM phosphate buffer; pH 7.4  
<sup>b</sup> 100 mM  
<sup>c</sup> 7 mM  
<sup>d</sup> The band was clearly multi-component

The presence of the different cations added to the PB did not result in significant shift (spectral resolution was 4 cm<sup>-1</sup>) of the amide I band in all the studied cases, both for the solution and the solid film spectra. This indicates that, in our experimental conditions, their influence on the peptide conformational equilibrium was negligible. Clearly, bandwidth is broader in the case of solution spectra, suggesting an equilibrium between several backbone conformations. Moving from solution to solid

film spectra, the amide I band significantly narrowed and shifted to higher wavenumbers in all the cases. However, while both hVDAC2(12-36) and hVDAC3(1-25) reached a value of  $1654\text{ cm}^{-1}$  (and a FWHM of ca.  $50\text{ cm}^{-1}$ ), hVDAC1(1-25) exposes slightly red shifted amide I maximum centered at  $1648\text{ cm}^{-1}$  with broader FWHM ( $61\text{ cm}^{-1}$ ).

### 3.1.3 *Nuclear magnetic resonance spectroscopy*

The N-terminal peptide of the three human isoforms of VDAC was investigated in PB. The  $^1\text{H}$  and  $^{13}\text{C}$  resonances were assigned on the basis of a set of two-dimensional experiments, namely DQF-COSY, TOCSY, NOESY and  $^1\text{H}$ - $^{13}\text{C}$ -HSQC as described by Cavanagh et al. <sup>38</sup>. Results are reported in table S1, S2 and S3 for hVDAC1(1-25), hVDAC2(12-36) and hVDAC3(1-25), respectively. The chemical shift index (CSI) values were calculated for both the  $\alpha$ -protons and  $\alpha$ -carbons, but deviation from the reference ‘random coil’ values were negligible and, in general, no peptide portions with specific CSI values were identified, indicating the absence of any well defined folded structure <sup>72-74</sup>. The experimental chemical shift values of  $^1\text{H}\alpha$ ,  $^1\text{H}\beta$ ,  $^{13}\text{C}\alpha$  and  $^{13}\text{C}\beta$  were also analyzed through the software TALOS+ in comparison to its high-resolution structural database <sup>41</sup>. In agreement with the CSI analysis, the majority of residues were either classified as ‘ambiguous’ (meaning that any specific secondary structure could be predicted with sufficient confidence) or located in highly dynamic portions of the peptide. The very few predictions ranked as ‘good’ were sparse along the peptide sequence such that a reliable secondary structure prediction was not possible. Nevertheless, it was quite interesting to find that the only exception was a cluster of three consecutive residues in the hVDAC2(12-36), namely K23, A24 and

A25. These residues are located exactly in the middle of the peptide sequence and their backbone conformation was estimated as helical with a very high consensus. In agreement, all the measured  $^3J_{\text{HNH}\alpha}$  scalar coupling constants were found in the range 6-8 Hz, often reflecting motional averaging of multiple conformations, but that of hVDAC2(12-36) A24 and A25, which was 3.5 Hz, indicative of a helical backbone<sup>38</sup>. Some differences between the three peptides were also observed in the dipolar through-space sequential correlations. Figure 11 schematically shows the observed sequential  $^1\text{H}$ - $^1\text{H}$ -NOESY cross peaks (NOEs). A different number of NOEs was observed for the three peptides under investigation, in the order hVDAC1(1-25) < hVDAC3(1-25) < hVDAC2(12-36). In the case of hVDAC1(1-25), only short range HN-H $\alpha$  (i,i+1) were identified. Several short range HN-HN (i,i+1) were assigned, in

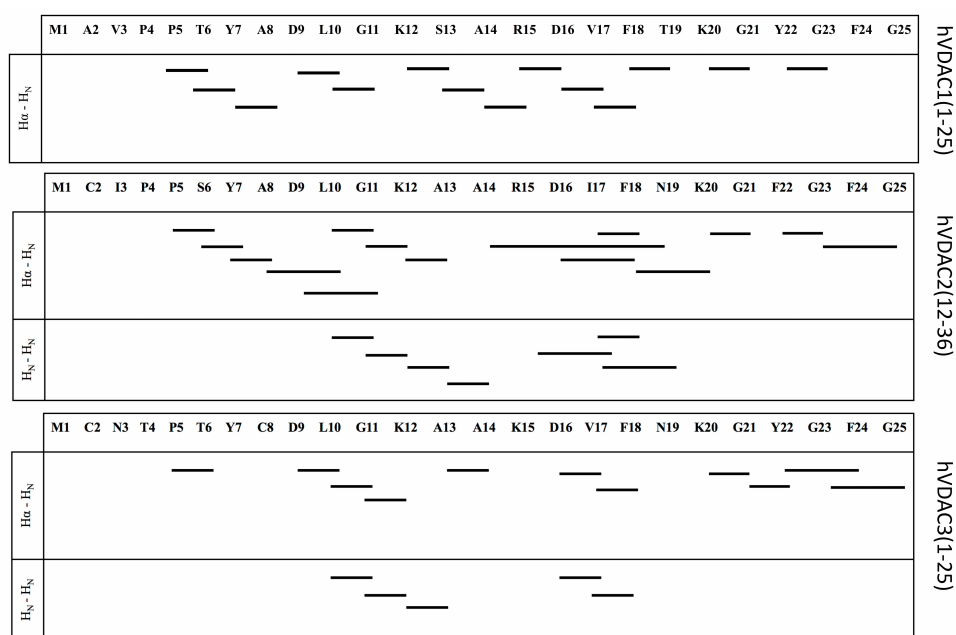


**Figure 11: Sequential inter-proton NOEs.** Proton-proton dipolar interactions found for hVDACs in 10 mM PB are reported as lines connecting the two residues involved.

addition, in the case of hVDAC3(1-25). Finally, hVDAC2(12-36) was characterized by a significantly higher number of NOEs. Both sequential HN-H $\alpha$  and HN-HN were found, either short range and several medium range.

#### 3.1.4 *Discussion of the spectroscopy results*

Far-UV CD spectroscopy is a commonly employed experimental technique to investigate proteins/peptides secondary structure<sup>36,75</sup>. Despite not providing high-resolution structural data, it gives valuable information on the proportions of different secondary structure motifs. For instance,  $\alpha$ -helical folding is characterized by three bands: an intense positive band at 192 nm and two negative bands at 208 and 222 nm, respectively.  $\beta$ -sheeted proteins/peptides are usually clearly distinguishable with their rather weak positive band at 195 nm and a similarly weak but negative band at 217 nm. The 'random coil' state, which is the absence of any well defined secondary structure, also has its characteristic CD spectral shape: an intense negative band at 198 nm. However, the latter is not easily distinguished from polyproline-like helices, which show an intense negative band at only slightly higher wavelength (~200 nm) and a very weak positive band at 215-230 nm<sup>36,75</sup>.

The spectra recorded in PB for both hVDAC1(1-25) and hVDAC3(1-25) are very similar to each other with a single negative band around 200 nm (Fig. 9), as already observed and reported in the literature for the hVDAC1(2-20) peptide<sup>76</sup>. At first glance, this result suggests that these two peptides are simply random coiled in PB, as it is usually observed for relatively short polypeptides, unless a suitable folding-promoting cosolvent or a lipid membrane model is present<sup>76-79</sup>. However, such negative band is actually located at wavelength significantly higher than 200 nm (Fig. 9), being compatible neither with a polyproline helix nor with a purely random coiled conformation. The case of hVDAC2(12-36) is more clear, with the deepest minimum shifted even far from 200 nm and the presence of at least one additional band around

220 nm. Its CD spectrum appears to result from two different contributions: the 'random coil', with its negative ellipticity at 200 nm, and the ' $\alpha$ -helix', with the two negative bands at 208 and 222 nm and the positive one at 192 nm, which partially cancels out the random coil negative band on the shortest wavelengths side (Fig. 9).

Two possible interpretations can be put forward:

- a) the peptide may have a rather short portion of its backbone folded as a stable helix, with the rest devoid of any defined secondary structure;
- b) the peptide exists in equilibrium between completely random coil states and partially folded states characterized by helical fragments of variable length.

The second hypothesis appears to be more probable in PB. Actually, a deeper analysis of the CD spectra for hVDAC1(1-25) and hVDAC3(1-25) suggests that the existence of an equilibrium applies also to these cases, if a relatively higher proportion of 'random coil' is taken into consideration.

All of the three hVDAC peptides resulted to be mostly unfolded in PB, but the existing equilibrium with a helical folding is seen and, in particular, such an intrinsic helical propensity is higher for the hVDAC2(12-36). When  $K^+$ ,  $Na^+$  or  $Mg^{2+}$  were added to the buffer, CD spectra did not show any dramatic change (Fig. 10), clearly indicating that hVDAC peptides helical propensity is not affected by these physiologically relevant ions. The slight differences and, in particular, the fact that a relatively low concentration of  $Mg^{2+}$  was sufficient to make the spectra of hVDAC1(1-25) and hVDAC3(1-25) comparable to those obtained for hVDAC2(12-36), is certainly interesting and suggests ion-specific effects on folding equilibria, but would require specific investigations<sup>80</sup>.

Infrared spectroscopy is often employed to investigate polypeptides conformation, with secondary structure determination through the analysis of the amide I band being

probably the most common application in the field of biopolymers<sup>81</sup>. This particular band is mostly due to the backbone C=O stretching vibration and is one of the most intense in the infrared spectrum of a polypeptide. It is sensitive to secondary structure as, for instance,  $\alpha$ -helix band is usually found at 1654  $\text{cm}^{-1}$  but it slightly shifts to lower wavenumbers with increasing the helix length or when the helix is bent. Short helical fragments (< 6 amino acid residues) can produce several bands throughout the amide I region (1620-1700  $\text{cm}^{-1}$ ), without giving rise to the typical  $\alpha$ -helical absorption.  $\beta$ -sheets can be easily distinguished, thanks to a strong band near 1630  $\text{cm}^{-1}$  and a weaker band near 1685  $\text{cm}^{-1}$ , whose precise position and separation help in discriminating parallel and antiparallel sheets<sup>81</sup>. In general, band position (for a given vibration mode) is slightly different for every possible conformer, thus, band broadening results from flexible structures making bandwidth informative as a measure of conformational plasticity.

In PB, the amide I band of the three hVDAC peptides resulted to be rather broad (table 1) presumably due to overlapping of multiple conformations, confirming the predominant random coil state in solution. Addition of different electrolytes to the buffer did not result in any significant change in the band position, confirming the CD results that indicated a negligible effect on the conformational equilibrium in solution. However, differences in the bandwidth were observed, again suggesting subtle ion-specific effects. Moving from solution to solid film spectra, the amide I band significantly narrowed, clearly indicating that peptides assumed a more rigid conformation upon dehydration and consequent adhesion to the diamond surface of the ATR device. Despite the presence of the different electrolytes, the band position was consistently found to be that typical of helical folding in all the cases. In the case of hVDAC1(1-25), however, a slightly lower wavenumber and a higher bandwidth

were found, suggesting a less regular and/or a bent helical folding. The information obtained from ATR complement those obtained from CD, and bolster the existence of a different conformational equilibrium between random coil and helical states for the three hVDAC peptides.

NMR is probably the most powerful technique to solve the 3D structure of proteins and peptides (together with X-ray crystallography, which is rarely applicable to short peptides). From coherent chemical shift deviations with respect to given reference values (the so-called 'random coil' values) and the measure of J-coupling constants, peptide secondary structure can be inferred<sup>38,72-74</sup>. Backbone  $\Phi$  and  $\Psi$  dihedral angles can be estimated to a rather high degree of confidence by comparing experimental data to the corresponding information available for peptides/proteins of known 3D structure, as implemented in the TALOS+<sup>41</sup>. Nuclei through-space distance can be obtained by measuring the relative intensity of the cross-peaks in NOESY spectra<sup>38</sup>. All these structural parameters can be finally applied as geometrical restraints within specific computer-assisted algorithms for 3D structure determination. However, usable parameters can be obtained only when the peptide under investigation has a sufficiently stable and defined conformation. The measured value of a chemical shift or a J-coupling constant is actually averaged by conformational mobility, i.e. they result to be the average over all the conformations visited during the NMR measurement. In the case of NOESY, conformational plasticity usually causes cross-peaks to be not observed at all<sup>38</sup>, such that, in general, the more the NOEs, the more structured the peptide.

In the present work,  $^1\text{H}$  and  $^{13}\text{C}$  chemical shift values were measured in PB for the N-terminal fragment of the three human isoforms of VDAC. The lacking of significant deviations from the 'random coil' reference values confirms the absence of any stable

and defined conformation<sup>72-74</sup>. This is also supported by the  $^3J_{\text{HNH}_\alpha}$  coupling constants in the 6-8 Hz range, indicative of motional averaging, and by the rather low number of NOEs observed in all cases (Fig. 8)<sup>38</sup>. However, the number of NOEs followed the order hVDAC1(1-25) < hVDAC3(1-25) < hVDAC2(12-36), suggesting a slight but significant difference in the conformational equilibrium. In addition, while dipolar interactions were observed only between adjacent residues in the case of hVDAC1(1-25) and hVDAC3(1-25), some medium range interactions were found for hVDAC2(12-36). Actually, only in the case of the latter we found three consecutive residues (K23, A24 and A25) having their chemical shift values compatible with a helical conformation, with two of them (A24 and A25) showing a  $^3J_{\text{HNH}_\alpha}$  coupling constant of 3.5 Hz, typical for helices. Nevertheless, for the sake of clarity, it has to be stressed that the 3D structure could not be determined in any case, since the number of NMR parameters was too low and motional averaging evident from our results. In agreement with both CD and IR spectroscopy, despite all hVDAC peptides were mostly random coiled in solution, a slight but significant difference among the three was consistently found. CD indicated that hVDAC2(12-36) has the highest helical propensity. IR suggested hVDAC1(1-25) as the one with the less regular structure upon dehydration. NMR supported the same trend of folding propensity: hVDAC2(12-36) > hVDAC3(1-25) > hVDAC1(1-25).

### 3.2 Structural characterization in-silico of the N-terminal domains of hVDACs

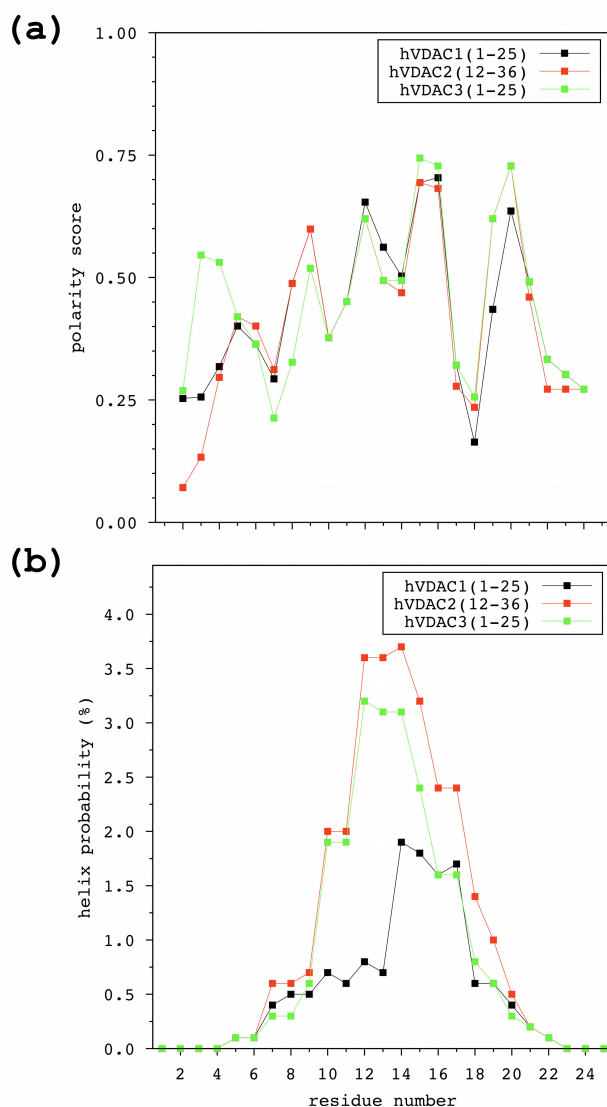


**Figure 12: Bioinformatic analyses.** Polarity score is shown (a) for the three peptides as a function of residue number. The higher the score, the more polar the amino acid residue is. Agadir prediction ( $T = 300\text{K}$  pH 7.4 ionic strength 0.1 M) is shown in (b) as helix percentage as a function of residue number.

#### 3.2.1 Bioinformatics analyses

Polarity score profile (figure 12a) shows that the more and less polar residues are alternated along the amino acid sequence. The pattern is absolutely comparable within the three hVDAC N-terminal peptides meaning that the alternation of the residue type is homologous. The largest differences have been found only at the very beginning of the sequences. The application of the Agadir algorithm

resulted in a rather low helix

probability in PB (figure 12b), with the three peptides sharing the same range of residues with a nonzero probability, i.e. 6-20. Despite values are low, the trend  $\text{hVDAC2}(12-36) > \text{hVDAC3}(1-25) > \text{hVDAC1}(1-25)$  is evident.

### 3.2.2 Molecular dynamics simulations

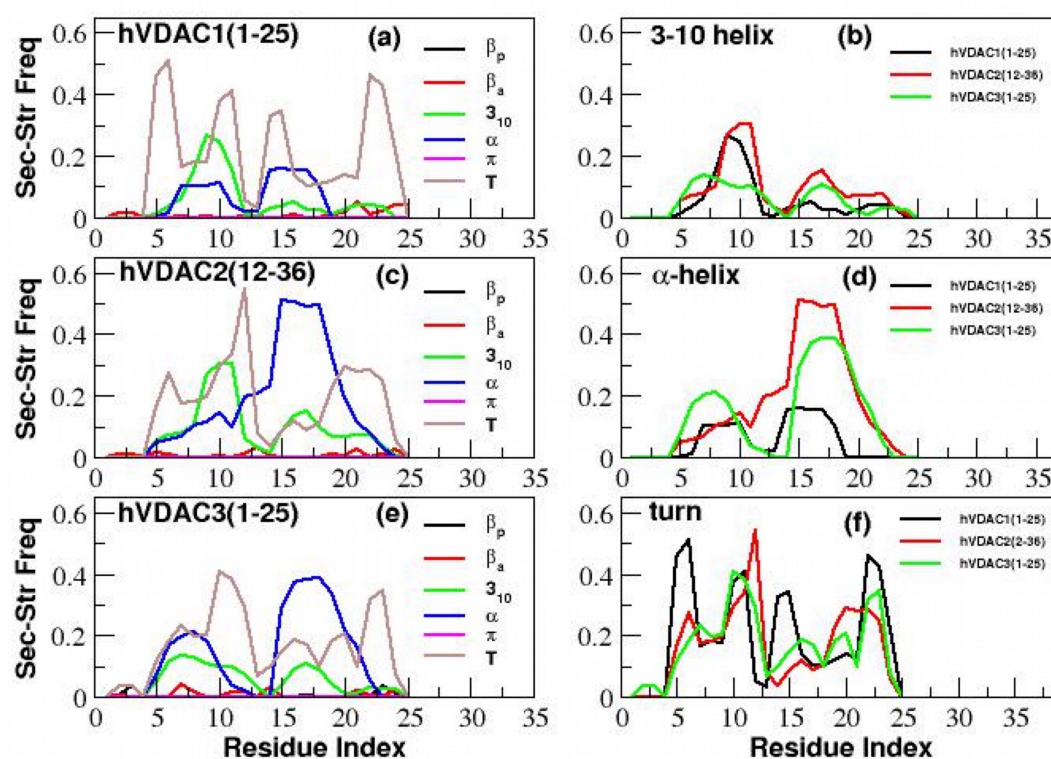


**Figure 13:** Secondary structure profile obtained for the N-terminal peptides of the three hVDAC isoforms. Panels (a), (c) and (e) show the frequency of all the investigated secondary structure motifs for hVDAC1(1-25), hVDAC2(12-36) and hVDAC3(1-25), respectively ( $\beta_p$ : parallel  $\beta$ -strand;  $\beta_a$ : antiparallel  $\beta$ -strand;  $3_{10}$ :  $3_{10}$ -helix;  $\alpha$ :  $\alpha$ -helix;  $\pi$ :  $\pi$ -helix; T:  $\beta$ -turn). In the panels (b), (d) and (f) the three peptides are directly compared with respect to the profiles of  $3_{10}$ -helix,  $\alpha$ -helix and  $\beta$ -turn, respectively.

Peptide secondary structure analysis was performed on the target replica using the DSSP algorithm<sup>69</sup>. This is based on the assignment of the backbone hydrogen bonding pattern to different secondary structure motifs, namely,  $\alpha$ -,  $\pi$ - and  $3_{10}$ -helix, parallel and antiparallel  $\beta$ -strand, and the  $\beta$ -turn. Figure 13 shows the frequency of these secondary structure elements along the amino acid sequence of the three peptides under investigation. Although the ‘random coil’ was the prevalent state for all the three hVDAC peptides, a significant occurrence of  $\alpha$ -helix,  $3_{10}$ -helix and  $\beta$ -turn was revealed. While in both hVDAC1(1-25) and hVDAC3(1-25) the  $\alpha$ -helix shows a profile with two peaks, one around the 8<sup>th</sup> and the second around the 16<sup>th</sup>

residue, hVDAC2(12-36) is characterized by a single wide peak in the  $\alpha$ -helix profile. Such a single peak has the maximum located around the 16<sup>th</sup> residue but covers the same range spanned by the distribution obtained for the other two peptides, without any breakage (figure 13d). On the other hand, the  $3_{10}$ -helix profile is comparable for the three peptides (figure 13b), with an asymmetric bimodal distribution where the peak on the N-terminus side is the most populated.

The data obtained from the DSSP were used to reconstruct the CD spectra of the three

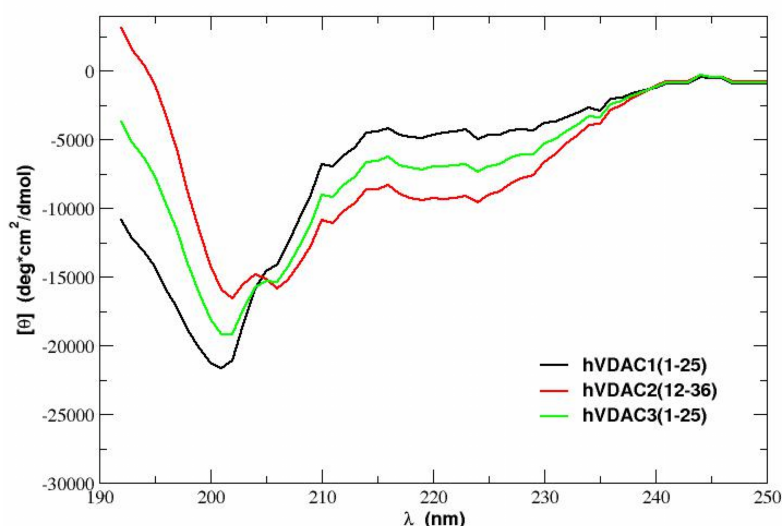


**Figure 14: Calculated CD spectra of the N-terminal peptides of the three hVDAC isoforms.** Reconstruction of spectra has been performed on the basis of the conformations visited along the trajectory of the target replica of the H-REMD simulation.

hVDAC peptides in order to compare them with the experimental ones, shown in figure 14. All the calculated CD spectra are characterized by a main negative band at a wavelength slightly higher than 200 nm. An additional negative band is present around 220 nm, which is more pronounced in the case of hVDAC2(12-36) but clearly detectable also in the spectra of both hVDAC1(1-25) and hVDAC3(1-25). In the latter cases, negative ellipticity was obtained in the 190-195 nm range, while slightly positive for hVDAC2(12-36). Interestingly, moving along the series hVDAC1(1-25), hVDAC3(1-25), hVDAC2(12-36), the more intense the negative band at ~220 nm, the more the main band at ~200 nm shifts to higher wavelength values and its intensity

decreases. By considering that  $\beta$ -type structure contribution was negligible in the CD spectra reconstruction, which was almost completely due to a different proportion of helical and random-coil fraction, it can be concluded that calculated spectra reflect the different helical content of the three peptides, with the following trend: hVDAC2(12-36) > hVDAC3(1-25) > hVDAC1(1-25).

### 3.2.3 *Discussion*

Helical propensity predictions by the software Agadir are in perfect agreement with the above-mentioned trend (Fig. 12)<sup>61-63</sup>. The overall helical propensity is low for each of the peptides, but this is not surprising considering that predictions are performed without taking into account the presence of any possible support for folding, like a lipid membrane model or a folding-promoting cosolvent (such as dodecylphosphocholine or trifluoroethanol). It is also very interesting to note that the range of nonzero helical propensity, residues 6 to 20, is in very good agreement with the folded portion observed in whole protein simulations<sup>82</sup>.

Molecular Dynamics simulations represent a powerful tool to complement the information provided by the experiments. Classical simulations in the canonical ensemble, however, are often non-ergodic and sample only a limited region of the phase space. This is due to the roughness of the protein conformation energy landscape that may easily lead to the system being trapped in a metastable minimum. In order to avoid this drawback we resorted to H-REMD simulations, where the exchanges among replicas allow the system to evade from kinetic traps.

The secondary structure analysis further confirmed that the three hVDAC peptides, although highly unordered in aqueous environment, have a significant intrinsic helical

content. In agreement with the experimental results, computer simulations revealed a clear ranking of helicity: hVDAC2(12-36) > hVDAC3(1-25) > hVDAC1(1-25). In particular, secondary structure profile of both  $3_{10}$ - and  $\alpha$ -helical conformation resulted to be highly asymmetric for all the hVDAC peptides (figure 13b, 13d). The main  $3_{10}$ -helix peak is located on the N-terminal region of the peptide sequence, with the highest values in the residue index range 6-12. On the other hand, the main  $\alpha$ -helix peak is located on the C-terminal side, with the highest values in the residue index range 13-20. This specific segregation of the  $3_{10}$ - and  $\alpha$ - contribution to the overall helicity is in very good agreement with the secondary structure profile obtained for the three peptides when simulated as part of the entire hVDAC channels<sup>82</sup>. This bimodal profile is also in remarkable agreement with the discontinuous nature of the N-terminal domain in different crystal structures available in the Protein Data Bank (PDB) on-line (<http://www.rcsb.org/pdb/home/home.do>), namely, in mouse VDAC1 (PDB entry 3EMN) and zebra fish VDAC2 (PDB entry 4BUM)<sup>22,30</sup>. The calculated CD spectra are in excellent qualitative agreement with the experimental ones (Fig. 9), bolstering the different equilibrium between random-coil and helical states for the three hVDAC N-terminal peptides.

### **3.3 Biophysical characterization of human VDAC channels**

In the following paragraphs, the comparative study on the entire channels will be presented. Firstly, the MD analysis of the conformation and ion diffusion through the pores. In particular, the first part will be focused on the analysis of the conformation of the N-termini within the whole channels whose results supported once more the

previous arguments. Finally, we will present and discuss the experimental characterization of the pores performed with electrophysiology.

### 3.3.1 *General Aspects*

Simulations were carried out both in the absence of KCl (apart from the few counterions needed to neutralize the system total charge) and in the presence of KCl 0.5 M. No transmembrane potential were applied in all the cases. KCl was the electrolyte of choice due to the almost equal diffusion coefficient of chloride and potassium ions in dilute solutions <sup>83</sup>. For small ions the translocation through a relatively large protein channel, such as the VDAC, is expected to depend on their mobility in water, the electrostatics of the lumen and protein dynamics. Thus, by using ions with comparable mobility, it is possible to focus on the properties of the protein. No significant differences were observed in the structural features and dynamics of each human VDAC isoform due to the presence of KCl 0.5 M in our simulations. Thus, the results obtained for the three proteins in the presence of KCl will be reported, compared and discussed hereinafter.

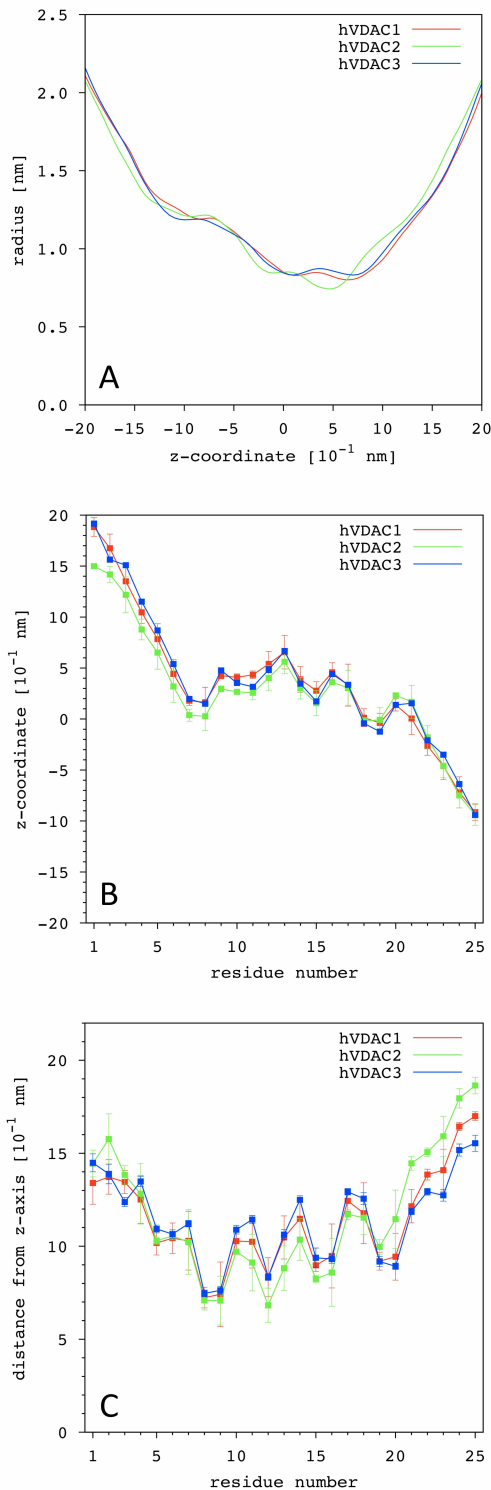


**Figure 15: Channel radius and position of the N-terminal domain inside VDAC lumen.** (A) Lumen radius calculated from solvent accessible area as a function of the z-coordinate for the three hVDACs. Protein channel is aligned and centered with respect to the z-axis, with both the N- and C-terminus located on the positive  $-z$  side of the lipid bilayer. (B) The z-coordinate and (C) the distance from the z-axis of the C $\alpha$ s is shown. Error bars were calculated as the standard deviation over 5 independent MD replicas. The residue 1'-11' of the hVDAC2 are not shown for the

Figure 15A shows the lumen radius as a function of the z-coordinate. In our simulations the protein is oriented along the z-coordinate with both the N- and C-terminus located on the positive-z side of the lipid bilayer. Recently, using intact cells, it has been demonstrated that the C-terminus faces the mitochondrial inter-membrane space<sup>84</sup>. All isoforms are not symmetric, with the positive-z half of the lumen characterized by a steeper decrease of the radius than the negative half. The absolute minimum is not located at  $z = 0$ , indeed, with both hVDAC1 and hVDAC3 having the minimum at  $z \sim 6.7$   $10^{-1}$  nm and a radius  $\sim 0.82$  nm, while it is located at  $z = 4.7$   $10^{-1}$  nm in hVDAC2 with a significantly lower radius of 0.74 nm. A second local

minimum close to the lumen center is present in all VDACs with a comparable value of  $\sim 0.83$  nm, whose precise location, again, is different for hVDAC2 ( $z = -1.0 \cdot 10^{-1}$  nm) with respect to the other two isoforms ( $z \sim 1.14 \cdot 10^{-1}$  nm).

### 3.3.2 *The N-terminal domain in the three isoforms*

The N-terminal domain of VDAC is considered a strategic asset for the stability and the functionality of the pore. It has been shown to be crucial for channel gating as well as for interaction with apoptosis related proteins<sup>6,17,25,26,28,29,31,33-35,85-87</sup>. The N-terminal domain has been observed to be characterized by a rather low flexibility, and a key role in stabilizing VDAC barrel in the open state has been put forward<sup>28,86-88</sup>.

In the hVDAC1 structure proposed by Bayrhuber, the N-terminal adheres to the barrel wall on the side of strands 8-15, located approximately at the midpoint of the hydrophobic portion of the membrane<sup>20</sup>. It is held by the hydrophobic interaction of residues 6 and 10 with 143 and 150, the very few hydrophobic residues directed towards the channel interior<sup>24,86,88,89</sup>. In addition, H-bonds contribute to facilitate its interaction with the interior wall of the pore<sup>22,28,89</sup>.

A close inspection of the amino acid sequence of the three human isoforms (Fig. 3) reveals intriguing differences. The hVDAC2 shows 11 residues not aligned with the sequence of hVDAC1 and hVDAC3 which will be referred to as 1'-11'. Furthermore different mutations are present in the N-terminal sequence. In particular, whereas hVDAC1 has no cysteines, both hVDAC2 and hVDAC3 are characterized by the presence of two cysteines in this protein region. It is not known whether they form any disulfide bridges with the other cysteines located in the barrel under physiological conditions in hVDAC2 or hVDAC3. This would clearly affect the N-terminal

mobility and, in turn, the flexibility of the barrel, and might represent a striking difference in the dynamics of the human isoforms of VDAC. In the present investigation, all cysteines were simulated in the reduced form: the molecular analysis of refolded VDAC2 suggested, indeed, that the cysteines do not form disulfide bridges<sup>90</sup>.

Another interesting difference among the sequence of the three hVDACs is the distribution and number of acidic and basic residues. Neglecting histidines, that are not charged in our simulations, all the three isoforms have a net positive charge: hVDAC1 has 32 basic residues and 29 acidic ones (net charge +3), hVDAC2 contains 30 basic and 29 acidic (net charge +1), hVDAC3 has 31 basic and 25 acidic (net charge +6). Mutations are present both in the loops and in the barrel strands, but the N-terminal sequence shows a remarkable conservation of the distribution of these residues with a prevalence of positive residues (Fig. 3).

Figures 15B-C show the position of the  $\alpha$ -carbons comprising the N-terminal fragment of the three hVDAC isoforms. Both the z-coordinate (15B) and the distance from the z-axis (15C) are shown. Residues 1'-11' of the hVDAC2 are not shown for the sake of clarity; they are exposed to the solvent outside the lumen. This is because such additional residues of hVDAC2, as said, are not aligned neither with the amino acid sequence of the other two isoforms (Fig. 3), nor with the mVDAC reference structure used as template for the homology modeling. Thus, the software used to generate the starting configuration of the three hVDACs did not apply any geometrical restraint on these residues. This resulted in their simple addition to the protein structure model according to a random coiled backbone conformation. Recently, the crystallographic structure of VDAC2 has been solved for zebra fish (PDB code 4BUM) at high resolution (2.8 Å), showing a very high similarity with

both the human and mouse VDAC1 3D structure <sup>30</sup>. The zebra fish VDAC2 amino acid sequence has 84% identity and 98% similarity with the human VDAC2, with the main differences located in the external loops. In agreement with the solved 3D structures, the N-terminal fragment crosses the lumen with helical folding from the residue 6 to 20 in all the isoforms, and is horizontally located close to the lumen center. In the hVDAC2, the first half of the folded fragment is characterized by slightly lower values for both the z-coordinate and the distance from the z-axis, providing an explanation for the different profile of the lumen radius vs z-coordinate obtained (Figure 15A). However, differences are only slight and might be due to some inaccuracies in the modeling of the very first residues of hVDAC2, by virtue of presence of the additional 11 amino acids commented above.

The hydrophaticity profile of the N-terminal sequence is conserved in the three human isoforms, with the folded part characterized by a similar pattern of alternate hydrophobic and hydrophilic residues. The comparison between this profile and the  $\alpha$ -carbons distance from the z-axis (figure 15C) clearly shows that the N-terminal domain directs the hydrophilic residues towards the lumen center and protects the hydrophobic ones from the water solvent by facing the channel wall, in agreement with previous experimental observations <sup>76</sup>.

In all the three isoforms the most hydrophilic residues are the number 12, 15, 16, 19 and 20, whose mutation has been shown to affect channel selectivity and voltage-gating <sup>85,91</sup>. Whereas the most hydrophobic ones are the number 10, 17 and 18. The only striking difference among the three VDAC isoform is given by residue 3 (V, I and N in hVDAC1, 2 and 3, respectively), which is markedly hydrophobic in both hVDAC1 and hVDAC2, while it is mutated into a strongly hydrophilic residue in hVDAC3.

This comparative study shows that all the three human isoforms share hydrophobic contacts between N-terminal domain and the few inward directed hydrophobic residues of the channel wall.

Secondary structure analysis of the N-terminal domain shows a high similarity among the three human isoforms of VDAC with a  $3_{10}$ -helix comprising the residues 6-12 and an  $\alpha$ -helix from residue 13 to 20. However a different plasticity was observed in the simulations. The hVDAC2 and hVDAC3 are comparable with a somewhat rigid  $\alpha$ -helical fragment and a low (~10%) occurrence for the ‘unstructured’ conformation in the  $3_{10}$ -helical portion. On the other hand, the N-terminal fragment of the hVDAC1 is characterized by a higher plasticity, with a ~20% occurrence for the ‘unstructured’ conformation throughout the folded segment. As far as the hVDAC2 is concerned, it is interesting to note the additional  $3_{10}$ -helical folded portion comprising residues 10’ to 3, which, being amphipathic, adheres to the barrel wall. This results in a slight tightening of the main folded part of the N-terminal fragment, as it is shown in more details hereinafter.

Position and orientation of the N-terminal fragment in the VDAC lumen do not only depend on its amphipathicity and hydrophobic contacts with the barrel wall, but also on specific hydrogen bonds<sup>22,28</sup>. Table 2 reports the H-bonds formed by the N-terminal fragment residues having an occurrence >20% in our simulations. All the three human isoforms of VDAC are characterized by the presence of the most stable H-bonds between the very first residues of the N-terminal fragment and residues located at the barrel border, namely, in the strands (or in the  $\beta$ -turns) 8-11. Despite this appears to be a conserved feature of all the three VDAC isoforms, the occurrence and the number of this kind of H-bonds resulted to be significantly lower in the case of hVDAC1 (Table 2). These results complement the secondary structure analysis. A

**Table 2.**<sup>a</sup> Hydrogen bonds formed by residues of the N-terminal fragment.

hVDAC1					hVDAC2					hVDAC3				
res.1	at.1	at.2	res.2	occ. <sup>b</sup> [%]	res.1	at.1	at.2	res.2	occ. <sup>b</sup> [%]	res.1	at.1	at.2	res.2	occ. <sup>b</sup> [%]
					R10'	H $\eta$	O $\epsilon$	E147	66.9 $\pm$ 8.7					
										M1	H	O $\delta$	D121	63.3 $\pm$ 1.8
A2	O	H	H122	41.7 $\pm$ 4.5	C2	O	H	C122	66.0 $\pm$ 4.3					
					C2	S $\gamma$	H	E147	54.7 $\pm$ 6.5					
					I3	O	H $\eta$	R174	44.3 $\pm$ 5.9	N3	H	O $\delta$	D121	42.0 $\pm$ 7.3
										N3	H $\delta$	O $\delta$	D121	28.7 $\pm$ 6.1
P4	O	H $\delta$	N124	41.9 $\pm$ 10.2	P4	O	H $\delta$	N124	35.7 $\pm$ 4.4	T4	H $\gamma$	O	R120	74.3 $\pm$ 10.8
										P5	O	H $\gamma$	S124	28.2 $\pm$ 8.6
<i>T6</i>	<i>H<math>\gamma</math></i>	<i>O<math>\delta</math></i>	<i>D9</i>	<i>50.9 <math>\pm</math> 24.0</i>	<i>S6</i>	<i>H<math>\gamma</math></i>	<i>O<math>\delta</math></i>	<i>D9</i>	<i>46.9 <math>\pm</math> 5.6</i>	<i>T6</i>	<i>H<math>\gamma</math></i>	<i>O<math>\delta</math></i>	<i>D9</i>	<i>89.0 <math>\pm</math> 2.0</i>
										<i>T6</i>	<i>H</i>	<i>O<math>\delta</math></i>	<i>D9</i>	<i>34.1 <math>\pm</math> 4.8</i>
<i>A8</i>	<i>O</i>	<i>H<math>\eta</math></i>	<i>R15</i>	<i>33.6 <math>\pm</math> 7.7</i>	<i>A8</i>	<i>O</i>	<i>H<math>\eta</math></i>	<i>R15</i>	<i>28.4 <math>\pm</math> 2.5</i>					
<i>D9</i>	<i>O<math>\delta</math></i>	<i>H<math>\eta</math></i>	<i>R15</i>	<i>36.1 <math>\pm</math> 15.8</i>										
<i>L10</i>	<i>O</i>	<i>H<math>\eta</math></i>	<i>R15</i>	<i>29.7 <math>\pm</math> 5.6</i>	<i>L10</i>	<i>O</i>	<i>H<math>\eta</math></i>	<i>R15</i>	<i>32.5 <math>\pm</math> 6.2</i>	<i>L10</i>	<i>O</i>	<i>H<math>\zeta</math></i>	<i>K15</i>	<i>26.1 <math>\pm</math> 1.3</i>
					<i>K12</i>	<i>H<math>\zeta</math></i>	<i>O<math>\delta</math></i>	<i>D16</i>	<i>35.8 <math>\pm</math> 4.7</i>					
<i>R15</i>	<i>O</i>	<i>H<math>\gamma</math></i>	<i>T19</i>	<i>37.1 <math>\pm</math> 11.9</i>	<i>R15</i>	<i>O</i>	<i>H<math>\delta</math></i>	<i>N19</i>	<i>24.9 <math>\pm</math> 3.8</i>					
D16	O $\delta$	H $\zeta$	K224	43.4 $\pm$ 20.0						D16	O $\delta$	H $\zeta$	K224	34.2 $\pm$ 7.3
<i>D16</i>	<i>O<math>\delta</math></i>	<i>H<math>\zeta</math></i>	<i>K20</i>	<i>26.9 <math>\pm</math> 2.4</i>	<i>D16</i>	<i>O<math>\delta</math></i>	<i>H<math>\zeta</math></i>	<i>K20</i>	<i>31.8 <math>\pm</math> 4.9</i>					
<i>V17</i>	<i>O</i>	<i>H<math>\eta</math></i>	<i>Y22</i>	<i>69.8 <math>\pm</math> 4.7</i>						<i>V17</i>	<i>O</i>	<i>H<math>\eta</math></i>	<i>Y22</i>	<i>65.8 <math>\pm</math> 5.0</i>
F18	O	H $\zeta$	K236	63.7 $\pm$ 2.8	F18	O	H $\zeta$	K236	65.6 $\pm$ 2.2	F18	O	H $\zeta$	K236	67.1 $\pm$ 11.9
G25	H	O	L275	68.8 $\pm$ 6.7	G25	H	O	V275	50.8 $\pm$ 8.0	G25	H	O	V275	53.3 $\pm$ 3.0
					G25	O	H	T49	28.2 $\pm$ 4.8	G25	O	H	T49	25.4 $\pm$ 2.9

<sup>a</sup> H-bonds involving two residues of the N-terminal fragment are reported in *italics*, in order to be distinguished from those involving one residue of the N-term and one of the barrel.

<sup>b</sup> Only H-bonds with an occurrence > 20% are reported. Error is given as the standard deviation over 5 independent MD replicas.

weaker anchoring of the N-terminal fragment and, in turn, a higher plasticity are observed for the hVDAC1 when compared to the other isoforms.

The conserved H-bond between F18 and K236 is also remarkable. It is located right at the end of the folded portion of the N-terminal fragment and contributes to stabilize its position and orientation inside the lumen. Almost all the models proposed in the literature for VDAC voltage-dependent gating involve some kind of more or less extended displacement of the N-terminal fragment, which, bearing a net positive charge, would sense the transmembrane voltage. Whether it ends up outside the lumen and completely exposed to the solvent, or bound to the membrane surface, or it even stays inside the pore, the interactions between the N-terminal fragment and the barrel play a fundamental role in stabilizing the open over the closed state of the channel, as it has been also shown by  $\beta$ -strand deletion experiments<sup>17,22,26,28,35,89,92</sup>.

### 3.3.3 *Channel breathing motions*

A comprehensive picture of the existing interconnection between the fluctuations of the N-terminal fragment and the channel walls is achieved by the  $\alpha$ -carbons correlation map. Figure 16 shows that, from a general point of view, the correlation map is very similar for the three hVDAC isoforms. A stripe of positive correlation spots is present between the N-terminal fragment and the residues in the  $\beta$ -strands 8-19 as expected (white straight line in figure 16A-C), due to the above mentioned interactions between the N-terminal domain and this side of the  $\beta$ -barrel.

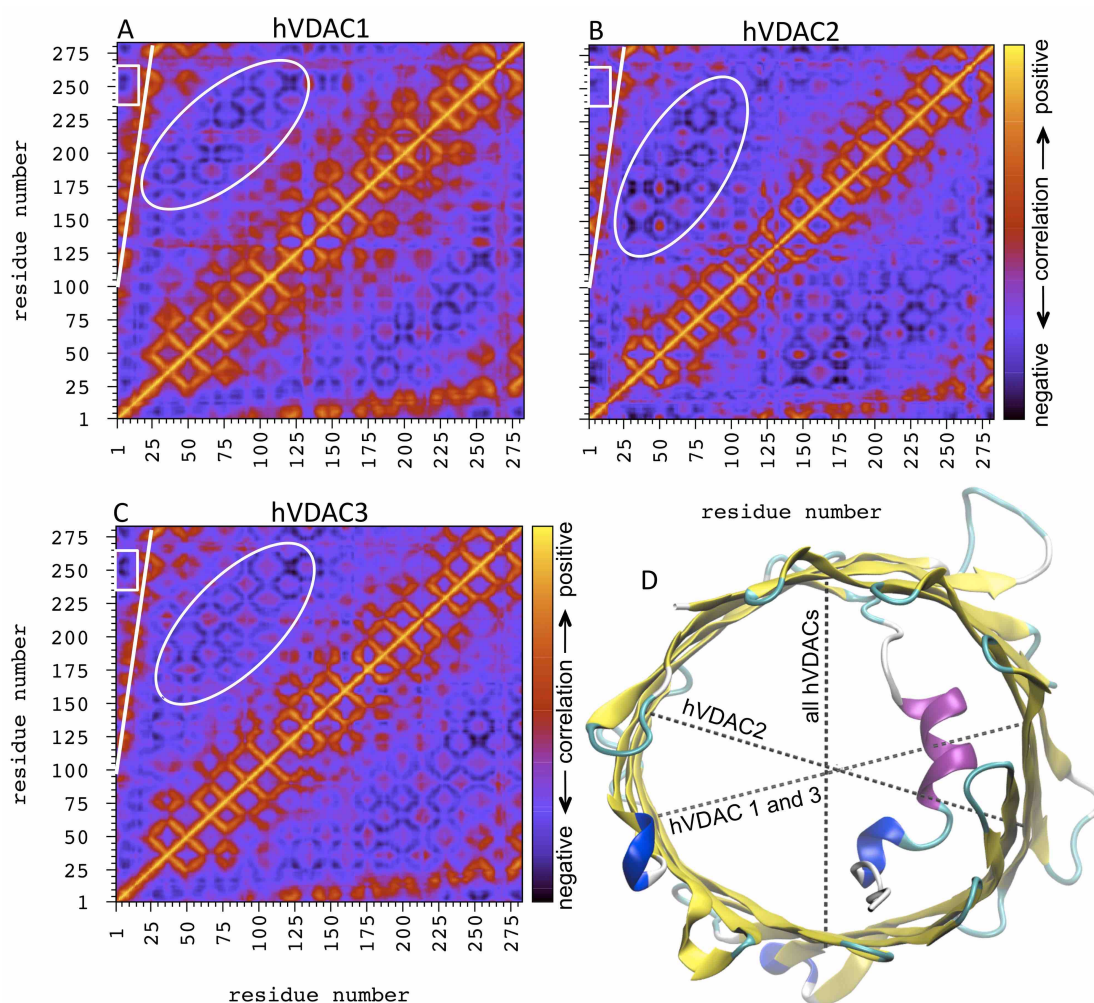


**Figure 16: Correlated fluctuations of hVDACs  $\beta$ -barrel.** Correlation map of  $\alpha$ -carbons fluctuations of (A) hVDAC1, (B) hVDAC2 and (C) hVDAC3. The map is color coded as reported in the box, moving from positive (yellow) to negative (dark blue) correlation. The positive correlation stripe between the N-terminal fragment and the portion of the barrel wall close to it, is indicated by the white straight line. The white oval circumscribes a series of anti-correlation spots between opposite sides of the barrel. The small white rectangle indicates the position of another interesting anti-correlation spot between the very beginning of the N-terminal fragment and the opposite side of the pore. (D) The corresponding axes (dashed lines) of maximal anti-correlation are shown for the three hVDAC isoforms using the structure of hVDAC1 as a template.

On the other hand, a clear anti-correlation spot is observed between the very beginning of the N-terminal fragment and the region around the residue 250 (the white rectangle in figure 16A-C), which corresponds to the opposite side of the pore with respect to the position where the N-terminus is H-bonded to the  $\beta$ -barrel, and is exactly located on the vertical defined by residue 25, i.e. where the N-terminal domain is linked to the first  $\beta$ -strand. In other words, a sort of anti-correlation axis

can be defined for all the hVDAC isoforms as reported in figure 16D, which, running longitudinally to the N-terminal direction through the lumen, connects the channel wall regions close to the beginning and the end of the N-terminal domain, respectively.

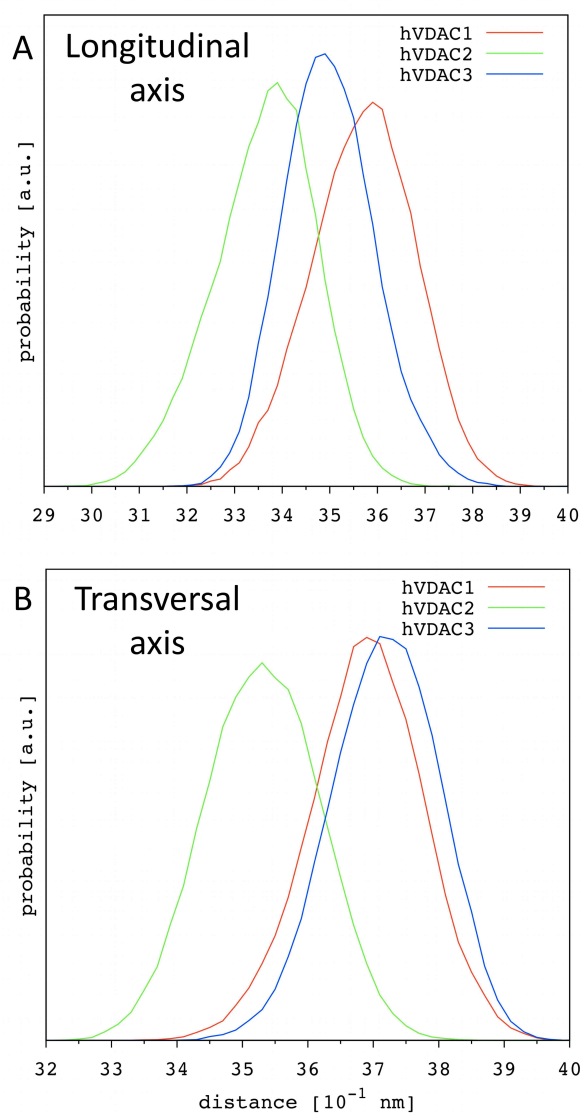


**Figure 17: Probability distribution of the two axes used to describe the elliptic shape.** Correlation analyses led to define two major axes of elliptic breathing motions of the  $\beta$ -barrel. The one is longitudinal the other is transversal to the N-terminal fragment direction through the pore. Probability distribution is shown for the (A) longitudinal and (B) transversal distance calculated at  $z \approx 0$  from 5 independent MD replicas for the three human isoforms.

Interestingly, almost all  $\beta$ -barrel residues showing a positive correlation with the N-terminal fragment, thus located in the  $\beta$ -strands 8-19, have a remarkable negative correlation with residues located on the other side of the channel, as shown by the series of anti-correlation spots indicated by the white oval in figure 16A-C. Thus, taking the central residues of the N-terminal fragment as reference and the corresponding  $\beta$ -barrel residues with the highest positive correlation, we looked for the maximum anti-correlation spots. This way, a second anti-correlation axis was identified for the three hVDAC isoforms as reported in figure 16D, which, running transversally to the N-

terminal direction through the lumen, connects opposite regions of the channel wall. As shown in figure 16D, the direction of this transverse axis is different for hVDAC2 with respect to hVDAC1 and hVDAC3.

The overall shape of the  $\beta$ -barrel cross-section can be described as elliptic with one axis longitudinal and one transversal to the N-terminal fragment. For each hVDAC isoform we conveniently chose a series of residues (their  $\alpha$ -carbon), at three different heights with respect to z-axis of the pore, to evaluate the length of these two axes as a function of simulation time. All isoforms are characterized by positive correlation between the axes with the same directionality, bolstering the analysis of the  $\alpha$ -carbons correlation map and showing that the barrel walls fluctuate almost uniformly throughout the z-coordinate. However, our analysis revealed that hVDAC2 has a significantly different dynamics. Fluctuations of the longitudinal and transversal axis of the pore are significantly anti-correlated in hVDAC1 and hVDAC3, whereas hVDAC2 shows almost any correlation between the two.

Recently, such an anti-correlated elliptical dynamics of the  $\beta$ -barrel has been proposed in the literature on the basis of an extensive computational and experimental investigation of hVDAC1<sup>28</sup>. The N-terminal domain was shown to have a relatively low mobility and to play a fundamental role in the modulation of  $\beta$ -barrel rigidity. Deletion of the N-terminal fragment led to a marked ellipticity of the channel wall (and higher fluctuations), mostly achieved through the shortening of the distance between  $\beta$ -strands 1 and 9, exactly corresponding to the 'longitudinal axis' defined in the present work. Correspondingly, a slight elongation of the transverse axis was observed. The authors concluded that elliptic deformation of the barrel is an essential component of voltage-gating and that changes in anion selectivity strictly depend on the specific shape of the channel (related to charges distribution inside the lumen)<sup>28</sup>.

Our structural characterization shows that such elliptic movements of the barrel are an intrinsic feature of all hVDAC isoforms but hVDAC2. Even in the presence of the N-terminal domain they are evident and represent the spontaneous breathing motions of this protein channel at equilibrium. Figure 17 shows the probability distribution of the length of both the longitudinal and transversal axis calculated for the three hVDACs. The longitudinal axes are in the order hVDAC1 > hVDAC3 > hVDAC2 (3.59, 3.49 and 3.39 nm, respectively; figure 17A). These results perfectly match the relative number and occurrence of the H-bonds formed between the very first N-terminal residues and the barrel reported above. The hVDAC2 showed the most stable interactions and its N-terminal fragment is characterized by the presence of an additional  $3_{10}$  helical portion adhering to the barrel wall. Its tighter N-terminal fragment forces the barrel longitudinal axis to shorter values than observed for the other two isoforms.

The transversal axes are in the order hVDAC3  $\approx$  hVDAC1 > hVDAC2 (3.72, 3.69 and 3.53 nm, respectively; figure 17B). In agreement with the correlation analyses, the transversal axis is found to be longer than the corresponding longitudinal one, showing that the overall shape of the channel is often slightly elliptical. Ellipticity values are in agreement with those reported in the literature for the wild-type hVDAC1<sup>28</sup>. Despite hVDAC2 has the shortest longitudinal axis among the three isoforms, it is not characterized by the longest transversal axis. This is not surprising, since no correlation has been found between the two distances in this case, but it is interesting to note that hVDAC2 results to be the more compact isoform with both the longitudinal and transversal axis being shorter, on average, than in the other two human isoforms. Definitely, a strong interplay between the N-terminal fragment flexibility and  $\beta$ -barrel motions emerged, in agreement with other observations

reported in the literature<sup>28,29</sup>. VDAC voltage-gating mechanism has been proposed to depend upon more or less extended movements of a highly charge portion of the protein<sup>25,26,28,29,31,33,85–87</sup>. Any motion of a charged mobile segment should occur along the direction of the electrical field applied<sup>93</sup>. Despite the present work was performed in the absence of any trans-membrane voltage, we can hypothesize that the switch to the closed state of VDAC is hindered if the N-terminus remains within the  $\beta$ -barrel. Thus, a movement of the N-terminal helix out of the lumen should be the very first step of the voltage-gating mechanism.

#### 3.3.4 *Ions passive translocation*

Table 3 summarizes the results obtained for the three hVDAC isoforms in the absence of transmembrane voltage. As expected from the literature, all the hVDACs resulted to be slightly selective for anions<sup>34,93,94</sup>.

The hVDAC1 and hVDAC3 are characterized by  $\text{Cl}^-/\text{K}^+$  selectivity ratio of 1.8, whereas hVDAC2 is less selective with a ratio of 1.4. The value of 1.8 found for hVDAC1 is in very good agreement with the values reported in the literature, obtained from both experimental and computational investigations on hVDAC1 and/or mVDAC1<sup>4,31,95</sup>. The lower average value obtained for hVDAC2 is in agreement with the experimental observation of two distinct populations for this particular isoform, one with similar conductance and selectivity to VDAC1, the other with a lower conductance and anion selectivity<sup>94,96</sup>.

From our simulations, this difference appears to be mostly due to a different overall affinity of hVDAC2 for chloride ions. On average,  $\sim 7.6$   $\text{Cl}^-$  have been found inside hVDAC1 and hVDAC3, while the hVDAC2 mean value was lower by  $\sim 1$  (Table 3).

Table 3.<sup>a</sup> **Ions translocation and selectivity in the absence of transmembrane voltage.**

		hVDAC1	hVDAC2		hVDAC3		
Cl <sup>-</sup> inside <sup>b</sup>		7.7 ± 0.2	6.8 ± 0.2		7.5 ± 0.3		
K <sup>+</sup> inside <sup>b</sup>		4.4 ± 0.3	4.9 ± 0.3		4.2 ± 0.2		
Anion selectivity <sup>c</sup>		1.7 ± 0.2	1.4 ± 0.1		1.8 ± 0.0		
Cl <sup>-</sup> to K <sup>+</sup> correlation <sup>d</sup>		+0.8 ± 0.1	+0.7 ± 0.1		+0.8 ± 0.0		
TRANSLOCATION EVENTS <sup>e</sup> (number of events; average time [ns])							
Cl <sup>-</sup>	ê	51 ± 6	2.2 ± 0.1	42 ± 8	2.0 ± 0.2	43 ± 5	2.2 ± 0.2
Cl <sup>-</sup>	é	44 ± 2	2.2 ± 0.3	40 ± 6	2.1 ± 0.2	49 ± 8	2.3 ± 0.2
K <sup>+</sup>	ê	16 ± 4	2.3 ± 0.4	19 ± 3	2.4 ± 0.5	20 ± 3	2.5 ± 0.3
K <sup>+</sup>	é	18 ± 5	2.2 ± 0.6	16 ± 2	3.1 ± 1.3	20 ± 4	2.1 ± 0.3
Permeation ratio <sup>f</sup>		2.8 ± 0.3	2.4 ± 0.2		2.3 ± 0.3		

<sup>a</sup> Error is given as the standard deviation over 5 independent MD replicas.

<sup>b</sup> Average number of ions per frame found inside the lumen ( $-18 \leq z \leq +18$ ).

<sup>c</sup> The time averaged ratio between Cl<sup>-</sup> and K<sup>+</sup> found inside the lumen.

<sup>d</sup> Cross-correlation coefficient between the number of Cl<sup>-</sup> and K<sup>+</sup> found inside the lumen as a function of simulation time.

<sup>e</sup> The arrow indicates the direction (z) of the translocation.

<sup>f</sup> The overall ratio between Cl<sup>-</sup> and K<sup>+</sup> translocation events.

On the other hand, the difference in the average number of K<sup>+</sup> found inside the lumen was smaller and at the limit of the statistical error of our simulations. A high positive correlation was found between the number of oppositely charged ions inside the lumen as function of simulation time, suggesting that channel affinity for Cl<sup>-</sup> and for K<sup>+</sup> are not mutually independent. Indeed, ion-pairing has been observed in previous computational investigations, and it has been put forward that K<sup>+</sup> needs Cl<sup>-</sup> to travel through the pore<sup>97</sup>.

Looking at the actual translocation events (table 3), there is no significant difference comparing the results obtained for the +z and -z direction in all the three hVDAC isoforms, thus, the Cl<sup>-</sup>/K<sup>+</sup> permeability ratio has been calculated taking the events

altogether into account. A slightly higher value is obtained for hVDAC1 than for the other two isoforms, even if the difference is at the limit of the statistical error of our simulation. The values found for the permeability ratio are in agreement with those reported in the literature <sup>98</sup>. A closer inspection of the overall number of Cl<sup>-</sup> and K<sup>+</sup> translocations reveals that, similarly to the number of ions found inside the lumen, the number of potassium events is comparable for all the isoforms, while hVDAC2 shows a lower number of chloride events than the other two hVDACs.

It is interesting to note that, for all the isoforms, no significant differences have been found in the average translocation time of Cl<sup>-</sup> and K<sup>+</sup> in both directions, suggesting a negligible difference in the overall translocation kinetics of the two ions and further supporting the major role played by channel affinity in anion-selectivity.

Figures 18A-C show the free energy profiles obtained for Cl<sup>-</sup> and K<sup>+</sup> in the three hVDAC isoforms. From a general point of view, the shape of the free energy profiles is comparable for the three proteins investigated as well as to the profiles reported in the literature <sup>95</sup>. Chloride is characterized by a mostly negative free energy with two wells at  $z \sim -10$  and  $+10$ , respectively, separated by a modest barrier. Potassium profile is somewhat complementary, being mostly positive and characterized by a sharp well at  $z \sim 0$  and two broad energy barriers around  $z \sim -10$  and  $+10$ , respectively. Chloride integrated  $\Delta G$  ( $-18 < z < +18$ ) follows the order hVDAC1  $\approx$  hVDAC3  $<$  hVDAC2 (-21.4, -19.5 and -14.7 kcal mol<sup>-1</sup> nm, respectively), which correlates with the opposite order found for the time-averaged number of Cl<sup>-</sup> inside the pore (table 3). Potassium integrated  $\Delta G$  follows the order hVDAC1  $\approx$  hVDAC3  $>$  hVDAC2 (+4.8, +5.2 and -2.7 kcal mol<sup>-1</sup> nm, respectively), which correlates with the opposite order found for the time-averaged number of K<sup>+</sup> inside the pore (table 3).

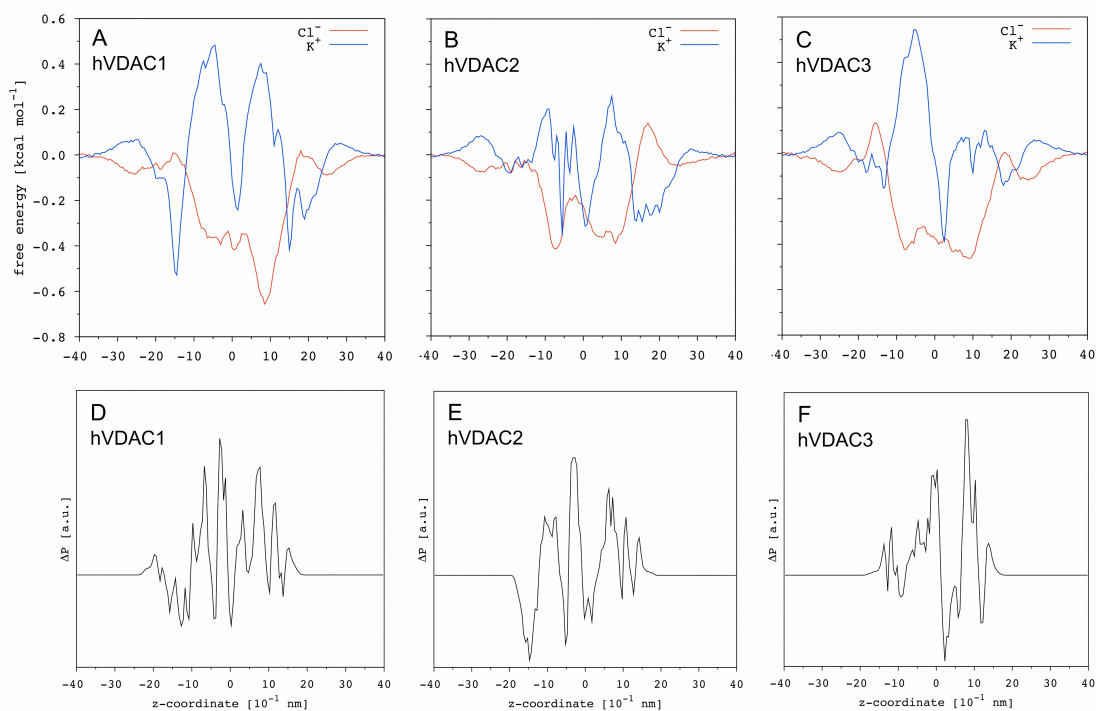


**Figure 18: Ions free energy profile and charged residues distribution.** Chloride and potassium profiles are shown for (A) hVDAC1, (B) hVDAC2 and (C) hVDAC3 as function of the z-coordinate. The statistical error estimated over 5 independent MD replicas is  $\sim 0.1$  kcal mol $^{-1}$ . In the panels (D-F) the difference  $\Delta Pz$  between the distribution of positively and negatively charged residues facing the protein lumen is reported as function of the z-coordinate.

For all the three isoforms, the difference between the height of the maximum energy barrier, taking either chloride and potassium and both directions into account, is  $\ll 1$  kcal mol $^{-1}$ . Indeed, any significant difference is observed between the average translocation time (Table 3). However, it is very informative to analyze and compare the specific differences between the free energy profiles obtained for the three hVDAC isoforms. On both sides of the channel ( $+30 > z > +20$ ;  $-20 > z > -30$ ), chloride experiences a free energy decrease upon approaching the protein, due to the overall net positive charge of the latter, while potassium shows a small barrier. On the contrary, at the lumen entrance ( $+20 > z > +15$ ;  $-15 > z > -20$ ), a small energy barrier is observed for chloride and a well for potassium. While these two barriers for chloride (and the two complementary potassium wells) have a comparable height in hVDAC1, the profile at the two entrances is not symmetric for hVDAC2 and hVDAC3.

The hVDAC1 has two negatively charged residues more than the positive ones at both entrances, explaining the comparable small free energy barrier for chloride. However, the number of charged residues at the entrances is not the same, the one at positive-z having 14 charged residues (8 negative and 6 positive), while the other has only 8 charged residues (5 negative and 3 positive). The energy barrier seems to be not determined by the number of charged residues per se, but mostly by the counterbalance between positively and negatively charged amino acid residues.

A stronger unbalancing at the positive-z entrance, with 7 negatively and only 4 positively charged residues characterize the hVDAC2 and, indeed, the barrier for chloride is higher on that side.

The case of hVDAC3 renders the importance of the ions balance clearer. Despite the equal number of positively and negatively charged residues at the two entrances, it has a higher chloride energy barrier at the negative-z entrance (Fig. 18C). Charged residues are not uniformly distributed in this case. One negative residue does not have a positive counterpart in its proximity resulting in local charge unbalance. Thus, while the net charge as function of the z-coordinate is certainly important in the determination of ions free energy profile, the charges distribution with respect to the x- and y-coordinate appears to be not negligible to achieve a comprehensive picture.

In an attempt to explain the differences observed among the three hVDACs, we first computed the distribution of positively and negatively charged residues along 'z' and then calculated the parameter  $\Delta P_z$  as the difference between the former and the latter (Fig. 18D-F). In the case of hVDAC1,  $\Delta P_z$  provides a quite convincing explanation for both chloride and potassium free energy profiles. Around  $z \sim +10$ ,  $\Delta P_z$  oscillates between  $\sim 0$  and positive values, explaining the presence of the deepest chloride well and a high barrier for potassium. Around  $z \sim -10$ ,  $\Delta P_z$  oscillates as well but shows

more negative values. Accordingly, the chloride well is less pronounced but, at the same time,  $\Delta P_z$  does not explain why the difference in the height of the two main energy barriers for potassium is negligible. Moving to hVDAC2 and hVDAC3 discrepancies are even more severe. For instance, the barrier separating the two main chloride wells in hVDAC2 corresponds to the highest positive peak of the  $\Delta P_z$  profile, such that one should expect a deep minimum. In the hVDAC3, as another example, the chloride well at  $z \sim -10$  corresponds to a pore section with  $\Delta P_z$  close to zero. Similarly,  $\Delta P_z$  does not justify the potassium profiles.

### 3.3.5 *Ions preferential localization inside the lumen*

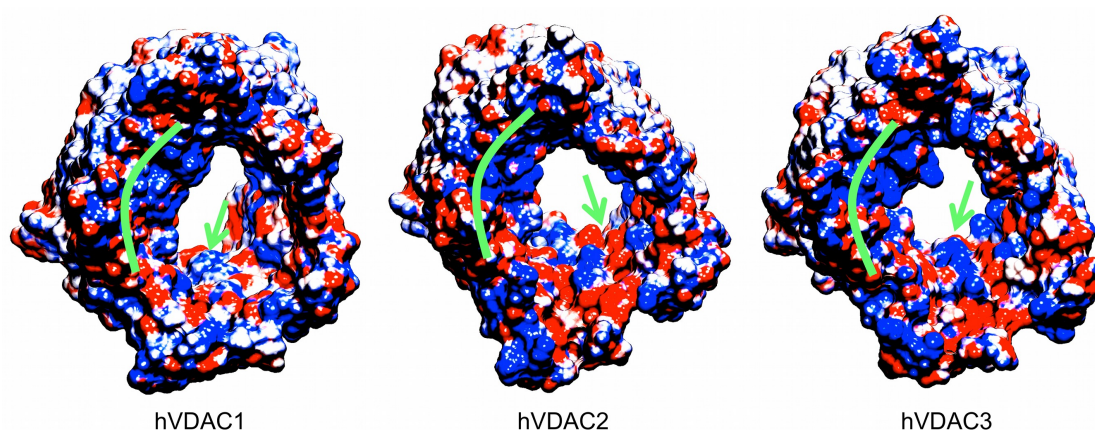


**Figure 19: Electrostatic potential surface.** The three isoforms are represented from the bottom with positive potential in blue and the negative one in red. The green line represents the position of the N-terminal fragment inside the lumen, whereas the green arrow indicates the area with the most remarkable differences.

Figure 19 shows the electrostatic potential surface for the three hVDAC isoforms (bottom view of the conformer obtained after the first 200 ns of NVT production run). The highest density of positive potential is observed around the structured segment of the N-terminal fragment. On the other hand, the highest density of negative potential is observed on the opposite side of the channel wall. These features are shared by the

three isoforms and are in agreement with results reported in the literature <sup>29,31</sup>. However, a remarkable difference was found in the central section of the channel on the side of  $\beta$ -strands 6-8, approximately halfway between the highest positive and the highest negative region. In particular, a mostly positive potential was found for hVDAC1 and hVDAC3, whereas a mostly negative potential was observed for hVDAC2.

A cluster analysis was performed on all the ions coordinates recorded along 5 independent MD replicas. Figure 6 shows both chloride and potassium clusters (occurrence  $\geq 20\%$ ) inside the three hVDAC isoforms. In each case, chloride ions resulted to be preferentially located in the middle of the pore, aligned along a sort of curved path around the N-terminal fragment. Potassium ions, on the other hand, have their main clusters localized at the periphery of the lumen, closer to the channel wall approximately in front of the N-terminal fragment. These results are in perfect agreement with the electrostatic potential surface of the hVDAC isoforms (Fig. 19): chlorides are preferentially located near the area with the highest density of positive potential, whereas potassium ions are preferentially found next to the channel wall with the highest density of negative potential. Similar observations are reported in the literature for the main isoform <sup>29,31</sup>.

However, both hVDAC1 and hVDAC3 are characterized by a double array of chloride clusters, one of the two being very close to the array of potassium, whereas only a single array of chloride clusters was observed in hVDAC2, such that chloride and potassium preferential localization appears to be more clear-cut in this case. This difference is particularly interesting and agrees with all of the above reported results. Indeed, the hVDAC2 is characterized by a lower anion selectivity than the other two isoforms (table 3), due to a significant reduction in chloride affinity. The localization

of the ‘missing’ chloride array strongly supports the major role played by the channel electrostatics, since it faces the area of the channel wall where a significant difference of the electrostatic potential has been observed (Fig. 19), differentiating hVDAC2 (more negative, thus repelling the chloride ions) from the other two isoforms (more positive).

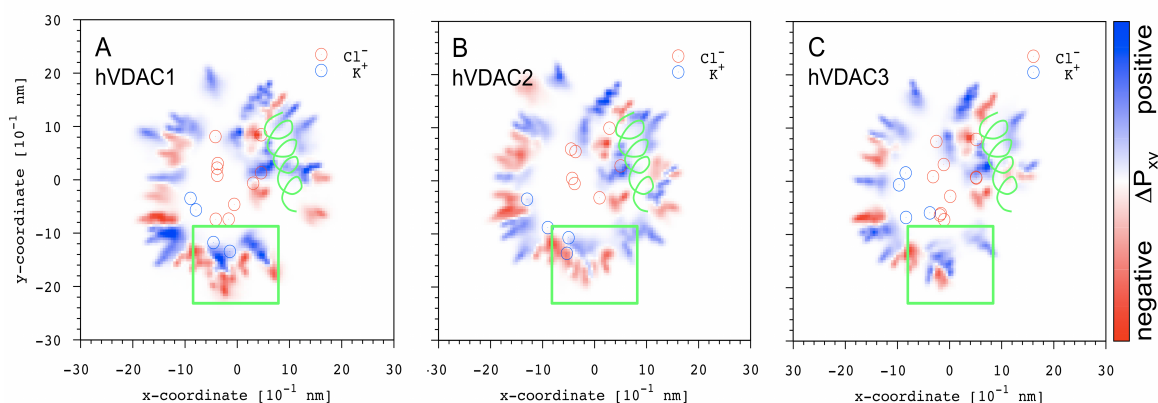


**Figure 20: Charged residues distribution on the xy-plane.** The difference  $\Delta P_{xy}$  between the distribution of positively and negatively charged residues on the xy-plane is shown for the three hVDAC isoforms. The green helix represents the N-terminal fragment crossing the lumen, whereas the green rectangle is used to highlight the region with the most striking difference between (B) hVDAC2 and (A, C) hVDAC1 and hVDAC3.

The parameter  $\Delta P_{xy}$  was calculated as the difference between the distribution of the positively and the negatively charged residues on the xy-plane. Figure 20 shows the results obtained for the three hVDAC isoforms together with the position of the ions clusters. The green rectangle highlight the area where the most striking difference was observed, in agreement with the electrostatic potential surface (figure 19). In the case of hVDAC2, positive density is significantly reduced when compared to the other two isoforms, one of the two chloride clusters arrays is missing and, in turn, segregation of the preferential localization of chloride and potassium ions is clear.

The residues lining each of the ion clusters were classified into different categories as reported in table 3. Chloride ions clusters are characterized by more positively charged residues than negative ones as expected, while potassium ions clusters are lined by an unexpected relatively high number of positively charged residues in all the

hVDAC isoforms. This difference is absolutely compatible with the different affinity observed for chloride and potassium ions and provide a valuable additional information to detail VDAC anion-selectivity. Our analysis has shown that a number of charged residues line both chloride and potassium clusters. If these ‘promiscuous’ residues are not taken into account, chloride clusters still have more positive than negative amino acids, while potassium clusters are characterized by more negatively than positively charged residues (table 3). The number of positive ‘promiscuous’ amino acids is higher than the negative ones, contributing to determine the overall selectivity for the anions. The difference between the number of these positive and negative ‘misplaced’ residues in hVDAC2 is significantly smaller than for the other two isoforms and, indeed, hVDAC2 is characterized by only one chloride clusters array, a more clear segregation between positive and negative ions inside the lumen, and a lower anion selectivity.

Finally, the presence of a relatively higher number of positively charged residues in the potassium clusters, than the negatively charged amino acids found in the chloride clusters, suggests that the cations need anions inside the lumen to counterbalance such positive residues. This is in agreement with where ion-pairing was investigated in detail, and provides a valid explanation for the high positive correlation we found between the time averaged number of  $\text{Cl}^-$  and  $\text{K}^+$  in the lumen (table 3) <sup>97</sup>.

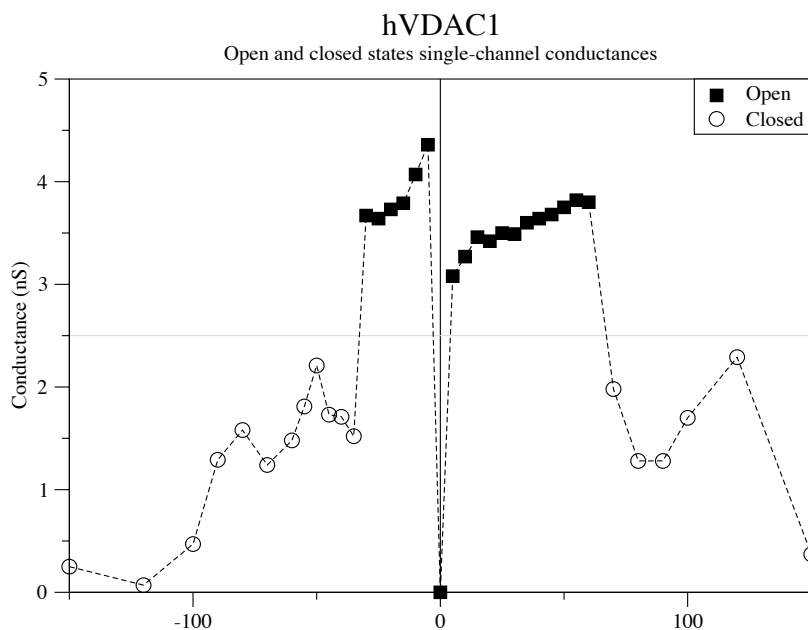


**Figure 21: Voltage versus conductance of hVDAC1.** The experiment has been performed used 1 M KCl and 10 mM HEPES at pH 7.2. Recordings have been acquired from -150 mV to + 150 mV.

### 3.3.6 *His-tag containing hVDACs*

Most of the knowledge on human VDAC isoforms is based mainly on the characterization of either hVDAC1 or the homologous murine VDAC1. The main feature concerning the activity of this channel is the particular gating occurring at low voltages that causes opening and partial closures of the pore and whose mechanism is not well understood. Being hVDAC1 the most characterized isoform, it was chosen as a probe to establish the experimental conditions in which the three isoforms would be compared and Figure 21 shows the conductance against the voltage for the most probable conductive states observed between -150 mV up to + 150 mV. One of the first traits that can be observed is the asymmetry of the conductance with respect to the polarity of the voltage; the channel is more conductive when negative voltages are applied (3.98 nS and 3.40 nS respectively). Also, another asymmetrical feature is the gating dependence on the polarity of the potential meaning that the channel relies mainly in a partial closed state at higher potentials (absolute value). In particular, in

the voltage range comprised between -20 mV and +35 mV the channel relies in an open state with a conductance of about 3.63 nS. It was observed that the number of conductive substate in which the channel may undergo is related to the value of the

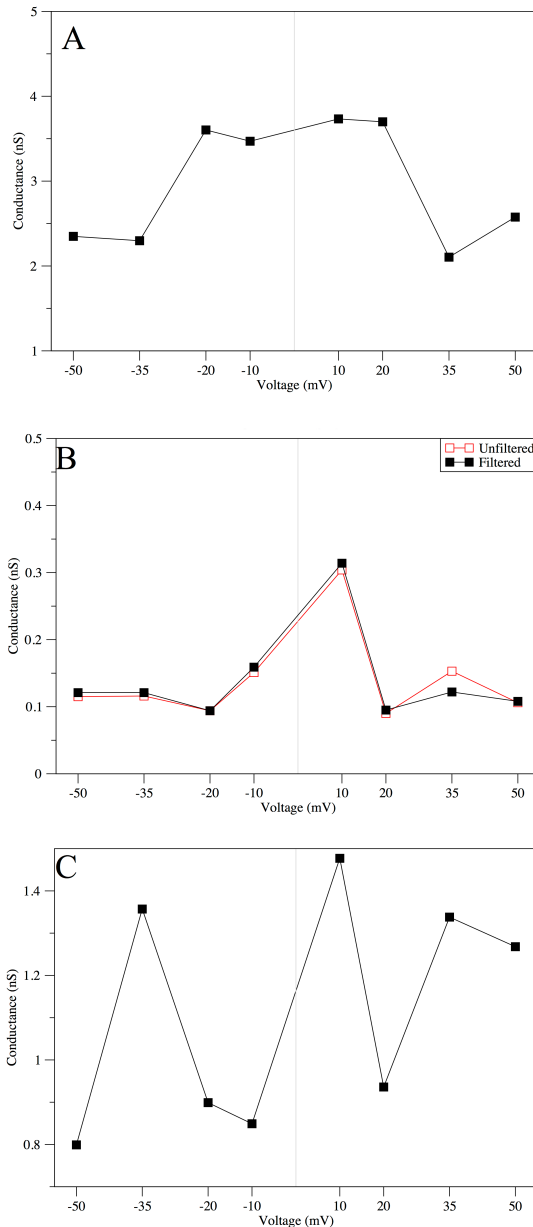


**Figure 22: Voltage versus conductance graphs of hVDAC isoforms.** Recordings have been performed using 1 M KCl and 10 mM HEPES at pH 7.2. (A) hVDAC1; (B) hVDAC2: a 2 kHz filter (black) has been applied on the recorded traces (red) and it is reported together with them in the inset. There is no significant difference in the conductances extrapolated from both traces except for the case of + 35 mV in which it was overestimated if unfiltered. (C) hVDAC3.

potential applied; the highest is the potential the highest is the number of substates. Indeed, the conductance values showed in Fig. 21 are the ones of the most occurring substate at a certain voltage. The asymmetry may be related to the chemico-physical properties of the channel and in particular to the electrostatics. In fact, as reported in Chapter 3.3.5.6 in this thesis, the channel shows a non-homogenous distribution of the charges along the lumen resulting in a different local polarity. Also, the asymmetrical behaviour can be used experimentally to determine the orientation of the channel within the single measurement. Starting from these observations, the comparison of the

human VDAC isoforms has been done applying  $\pm 10$  mV and  $\pm 20$  mV (fully open channel),  $\pm 35$  mV (polarity dependent closing) and  $\pm 50$  mV (closed

channel). Figure 22 shows the single channel conductances of the three isoforms. It is noticeable that the three isoforms behave differently despite their high sequence homology resulting in the following trend:

$$G_1 > G_3 > G_2$$

indicating with G the conductance. It can be generally stated, for all the isoforms, that the partial closures lead to the halving of the conductance (table 4).

Except for the conductance, though, also a different gating occurs suggesting that the isoforms may functionally assume different roles. In particular, hVDAC3 showed the most particular response to voltage, switching from open to closed substates more easily than the other isoforms. hVDAC2, whose traces were characterized by a high level of noise, relied mainly in a very low conductive state.

**Table 4: Average conductances of hVDACs in both the open and the most occurring closed states (1 M KCl 10 mM HEPES pH 7.2).**

	Conductance (nS)	
	Open state	Closed state
hVDAC1	3.7	2.4
hVDAC2	0.3	0.1
hVDAC3	1.3	0.9

This is in contrast with what has been published by Gattin et al. according to whom the conductance of the open channel is 3.79 nS<sup>99</sup>. This difference has been correlated to the position of the His-tag that is linked to the N-terminus in our case and to the C-terminus in Gattin et al.<sup>99</sup>. The influence of the His-tag on the electrophysiological activity has always been argued but there is not a comprehensive study on whether and how it can actually modify it or not. In the case of hVDAC2, at least, it seems to have a huge influence on the activity of the pore. In fact, the presence of the histidines residues in the N-terminus of hVDAC2 may provoke a further closure of the channel.

While, when linked to the C-terminus they are most probably exposed to the solvent not disturbing the electrophysiological activity.

As mentioned above, the basal activity of hVDAC1 consists of two main features: the partial closures of the channel at low voltages and the related gating characterized by the occurrence of unstable conductive states visited by the channel whenever a certain voltage is applied. The latter meaning that whilst many porins, e.g. OmpF, stabilizes in the closed state when a very high voltage is applied, hVDAC is able to “switch” on and off during the recording. This behaviour can be related to the high dynamicity of the solvent-exposed loops and to the flexibility of the pore itself whose breathing motions have been previously characterized<sup>82</sup>. Within these motions, the pore shrinks and expands restricting the diameter and resulting in lower ions flowing across the lumen. The observation of the closures at high voltages (in particular  $\pm 35$  mV and  $\pm 50$  mV) can be assumed as a higher dynamicity pumped by a faster flow of ions.

Previous studies showed that high concentration of ATP reduced the conductance of the pore partially blocking it<sup>7,100</sup>. However, the concentrations used in the above mentioned paper cannot be related to the physiological conditions. For this reason, the effects of low concentration of ATP have been studied. In particular the following concentrations have been used: 100  $\mu$ M, 200  $\mu$ M, 500  $\mu$ M, 1 mM and 2 mM. Indeed, the maximum concentration of ATP in the cell cytoplasm is 2 mM.

The gating of the channel, or rather the occurrence of different conductive states is already observable at 100  $\mu$ M in which a closed state starts to be “visited” at  $\pm 20$  mV. However the open state at low voltage ( $\pm 10$  and  $\pm 20$ ) is most relevant. Also, the dynamicity of the channel is affected by the small amount of ATP present in the bath and this is reflected by the mean value of the current at each voltage. Whilst an intermediate value of the current was observed in absence of ATP, the mean values

for the high voltages in presence of  $100\mu\text{M}$  of the substrate is shifted to the closed state values (Fig. 23).

The main trend that has been observed concerns the stability of both the fully open and the fully closed state. Either in absence or at high concentration of ATP the above mentioned states are stable. From  $100\mu\text{M}$  up to  $500\mu\text{M}$  the stability of those states is

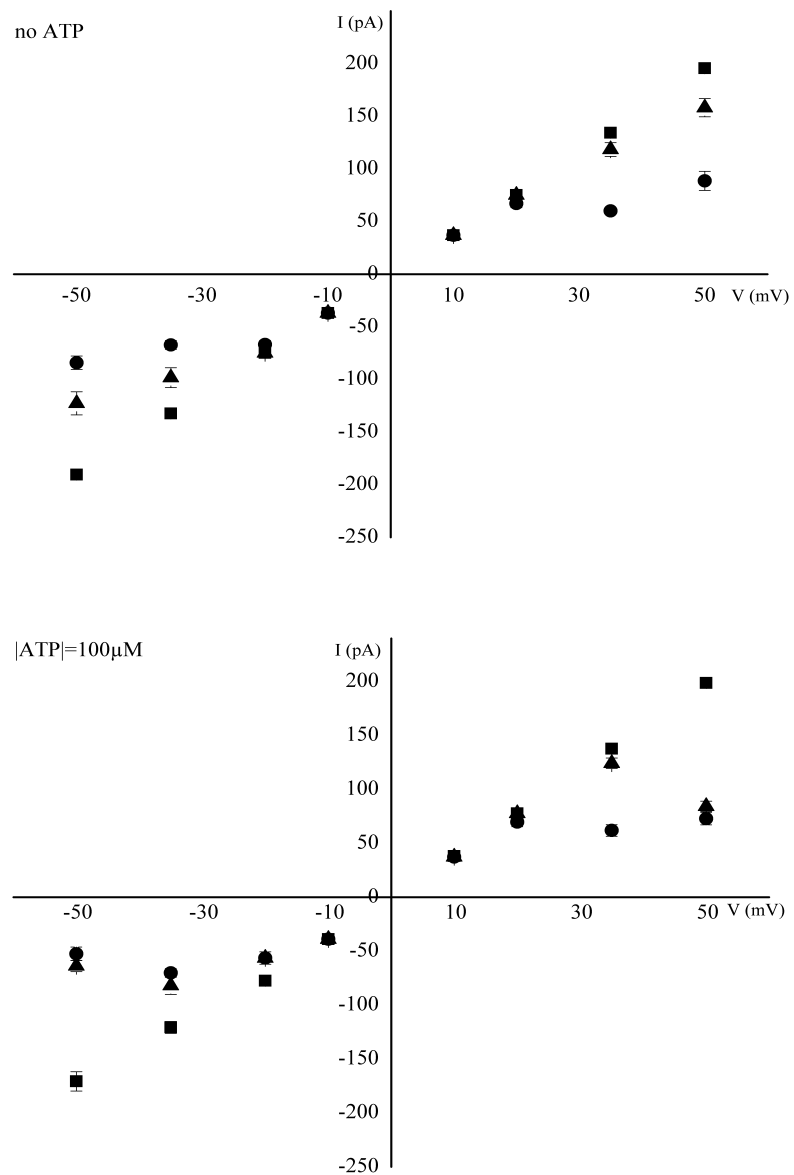


**Figure 23: I/V curves of hVDAC1 either in absence and in presence of  $100\mu\text{M}$  of ATP.** Square: average current of the open state; Triangle: the average of the most occurring state within the recordings; Circle: average current of the closed state.

compromised. Also, the number of substates increases together with the concentration of the substrate.



## Chapter 4 Conclusions and outlook

A comparison on the three human VDAC isoform has been done within this PhD thesis representing something new with respect to the previous studies. Even if the combination of both computational and experimental methods is not a novelty, the use of them in this study is much wider and complementary. The innovation of this work also relies on the comparison of the human isoforms for which literature is still lacking.

As mentioned in the introduction, the role of the N-termini within the whole porin has always been doubted. This was also due to the different hypothesis concerning its localization resulting from the different structures that have been proposed for VDAC1. With the structural study in buffer performed in this thesis, we were able to exploit how the N-termini domains of VDACs possess an intrinsic propensity to refold into a helical secondary structure. This supports the hypothesis according to whom this fragments rely inside the lumen of the pore modulating the gating activity and selectivity. The latter feature is related to the presence of positively charged lysines alternatively with hydrophobic residues that anchor the N-termini to the  $\beta$ -barrel. Furthermore, these experimental results were confirmed with the biophysical characterization of the channels. The MD simulations of the pores showed how the flexibility of the lumen walls occurs in a manner of breathing motions. These breathing motions, affecting the narrowing of the pore diameter, occur in harmony with the N-termini whose hydrophobic residues interact with a hydrophobic section of the lumen. The determination of the conductances of the channels through electrophysiology also supported the hypothesis of the N-termini inside the lumen. This was pointed out above all with hVDAC2 whose conductance was strongly

affected by the presence of 6 further histidines at the N-terminus. Nevertheless, the results obtained for hVDAC1 are consistent with the reported observations in literature. The novelty of the work performed in this thesis relies in the fact that a systematic comparison on the three human isoforms of VDAC has been before. Moreover, we were able to show that even low concentrations of ATP (in a physiological range) can stabilize hVDAC1, most likely by interacting with the external loops connecting the  $\beta$ -strands.

Although, in order to achieve a more accurate and consistent characterization of this channels, the His tags should be removed. For this reason, the wild-type isoforms have been cloned and expressed in *Escherichia coli*. Despite good results in the purification, the activity of the purified samples was not good enough to allow the characterization in the artificial bilayers. This can be correlated to the refolding of the channels whose protocol may need to be optimized.



## References

1. Werkheiser, W. C. & Bartley, W. The study of steady-state concentrations of internal solutes of mitochondria by rapid centrifugal transfer to a fixation medium. *Biochem. J.* **66**, 79–91 (1957).
2. Schein, S. J., Colombini, M. & Finkelstein, A. Reconstitution in planar lipid bilayers of a voltage-dependent anion-selective channel obtained from paramecium mitochondria. *J. Membr. Biol.* **30**, 99–120 (1976).
3. Colombini, M. Purification of VDAC (voltage-dependent anion-selective channel) from rat liver mitochondria. *J. Membr. Biol.* **74**, 115–21 (1983).
4. Benz, R. Permeation of hydrophilic solutes through mitochondrial outer membranes: review on mitochondrial porins. *Biochim. Biophys. Acta* **1197**, 167–196 (1994).
5. Colombini, M. VDAC: the channel at the interface between mitochondria and the cytosol. *Mol. Cell. Biochem.* **256-257**, 107–115 (2004).
6. Shoshan-Barmatz, V. *et al.* VDAC, a multi-functional mitochondrial protein regulating cell life and death. *Mol. Aspects Med.* **31**, 227–285 (2010).
7. Rostovtseva, T. & Colombini, M. VDAC Channels Mediate and Gate the Flow of ATP : Implications for the Regulation of Mitochondrial Function. *Biophys. J.* **72**, 1954–1962 (1997).
8. Messina, A., Reina, S., Guarino, F. & De Pinto, V. VDAC isoforms in mammals. *Biochim. Biophys. acta - Biomembr.* **1818**, 1466–1476 (2012).
9. Bathori, G. *et al.* Novel aspects of the electrophysiology of mitochondrial porin. *Biochem. Biophys. Res. Commun.* **243**, 258–263 (1998).
10. Beutner, G., Ruck, A., Riede, B. & Brdiczka, D. Complexes between

- hexokinase, mitochondrial porin and adenylate translocator in brain: regulation of hexokinase, oxidative phosphorylation and permeability transition pore. *Biochem. Soc. Trans.* **25**, 151–157 (1997).
11. Rostovtseva, T. K. & Bezrukov, S. M. VDAC inhibition by tubulin and its physiological implications. *Biochim. Biophys. Acta* **1818**, 1526–35 (2012).
  12. De Stefani, D. *et al.* VDAC1 selectivity transfers apoptotic Ca<sup>2+</sup> signals to mitochondria. *Cell Death Differ.* **19**, 267–273 (2012).
  13. Cheng, E. H. Y., Sheiko, T. V., Fisher, J. K., Craigen, W. J. & Korsmeyer, S. J. VDAC2 inhibits BAK activation and mitochondrial apoptosis. *Science (80- )*. **301**, 513–517 (2003).
  14. Huizing, M., Ruitenbeek, W., Thinner, F. & De Pinto, V. Deficiency of the voltage-dependent anion channel (VDAC): a novel cause of mitochondrial myopathies. *Lancet* **344**, 1206–1210 (1994).
  15. Tomasello, F. M. *et al.* Outer membrane VDAC1 controls permeability transition of the inner mitochondrial membrane in cellulo during stress-induced apoptosis. *Cell Res.* **19**, 1363–1376 (2009).
  16. Rostovtseva, T. K. *et al.* Bid, but not Bax, regulates VDAC channels. *J. Biol. Chem.* **279**, 13575–13583 (2004).
  17. Shoshan-barmatz, V., Keinan, N., Abu-hamad, S., Tyomkin, D. & Aram, L. Biochimica et Biophysica Acta Apoptosis is regulated by the VDAC1 N-terminal region and by VDAC oligomerization : release of cytochrome c , AIF and Smac / Diablo. *BBA - Bioenerg.* **1797**, 1281–1291 (2010).
  18. Maldonado, E. N. & Lemaster, J. J. Warburg revisited: regulation of mitochondrial metabolism by voltage-dependent anion channels in cancer cells. *J. Pharmacol. Exp. Ther.* **342**, 637–641 (2012).

19. De Pinto, V., Reina, S., Guarino, F. & Messina, A. Structure of the voltage dependent anion channel: state of the art. *J. Bioenerg. Biomembr.* **40**, 139–147 (2008).
20. Bayrhuber, M. *et al.* Structure of the human voltage-dependent anion channel. *Proc. Natl. Acad. Sci. U. S. A.* **105**, 15370–15375 (2008).
21. Hiller, S. *et al.* Solution structure of the integral human membrane protein VDAC-1 in detergent micelles. *Science (80-. ).* **321**, 1206–1210 (2008).
22. Ujwal, R. *et al.* The crystal structure of mouse VDAC1 at 2.3 Å resolution reveals mechanistic insights into metabolite gating. *Proc. Natl. Acad. Sci. U. S. A.* **105**, 17742–17747 (2008).
23. Schulz, G. E. Beta-barrel membrane proteins. *Curr. Opin. Struct. Biol.* **10**, 443–447 (2000).
24. Hiller, S. & Wagner, G. The role of solution NMR in the structure determinations of VDAC-1 and other membrane proteins. *Curr. Opin. Struct. Biol.* 396–401 (2009). doi:10.1016/j.sbi.2009.07.013
25. Colombini, M. The published 3D structure of the VDAC channel: native or not? *Trends Biochem. Sci.* **34**, 382–9 (2009).
26. Tejjido, O. *et al.* Affixing N-terminal  $\alpha$ -helix to the wall of the voltage-dependent anion channel does not prevent its voltage gating. *J. Biol. Chem.* **287**, 11437–11445 (2012).
27. Hiller, S., Abramson, J., Mannella, C., Wagner, G. & Zeth, K. The 3D structures of VDAC represent a native conformation. *Trends Biochem. Sci.* **35**, 514–21 (2010).
28. Zachariae, U. *et al.*  $\beta$ -Barrel Mobility Underlies Closure of the Voltage-Dependent Anion Channel. *Structure* **20**, 1540–1549 (2012).

29. Rui, H., Lee, K. Il, Pastor, R. W. & Im, W. Molecular dynamics studies of ion permeation in VDAC. *Biophys. J.* **100**, 602–10 (2011).
30. Schredelseker, J. *et al.* High resolution structure and double electron-electron resonance of the zebrafish voltage-dependent anion channel 2 reveal an oligomeric population. *J. Biol. Chem.* **289**, 12566–77 (2014).
31. Choudhary, O. P. *et al.* The electrostatics of VDAC: implications for selectivity and gating. *J. Mol. Biol.* **396**, 580–92 (2010).
32. Song, J., Midson, C., Blachly-Dyson, E., Forte, M. & Colombini, M. The sensor regions of VDAC are translocated from within the membrane to the surface during the gating processes. *Biophys. J.* **74**, 2926–2944 (1998).
33. Mannella, C. a. Conformational changes in the mitochondrial channel protein, VDAC, and their functional implications. *J. Struct. Biol.* **121**, 207–18 (1998).
34. Shoshan-Barmatz, V. & Ben-Hail, D. VDAC, a multi-functional mitochondrial protein as a pharmacological target. *Mitochondrion* **12**, 24–34 (2012).
35. Abu-Hamad, S. *et al.* The VDAC1 N-terminus is essential both for apoptosis and the protective effect of anti-apoptotic proteins. *J. Cell Sci.* **122**, 1906–1916 (2009).
36. Kelly, S. M. & Price, N. C. The use of circular dichroism in the investigation of protein structure and function. *Curr. Protein Pept. Sci.* **1**, 349–84 (2000).
37. Wüthrich, K., Billeter, M. & Braun, W. Polypeptide secondary structure determination by nuclear magnetic resonance observation of short proton-proton distances. *J. Mol. Biol.* **180**, 715–740 (1984).
38. Cavanagh, J. *Protein NMR Spectroscopy: Principles and Practice.* Elsevier Academic Press **2nd**, (2007).
39. Ogg, R. J., Kingsley, P. B. & Taylor, J. S. WET, a T1- and B1-insensitive

- water-suppression method for in vivo localized  $^1\text{H}$  NMR spectroscopy. *J. Magn. Reson. B* **104**, 1–10 (1994).
40. Smallcombe, S. H., Patt, S. L. & Keifer, P. A. *WET Solvent Suppression and Its Applications to LC NMR and High-Resolution NMR Spectroscopy. Journal of Magnetic Resonance, Series A* **117**, (1995).
  41. Shen, Y., Delaglio, F., Cornilescu, G. & Bax, A. TALOS+: a hybrid method for predicting protein backbone torsion angles from NMR chemical shifts. *J. Biomol. NMR* **44**, 213–23 (2009).
  42. Benz, R., Janko, K., Boos, W. & Lauger, P. Formation of large, ion-permeable membrane channels by the matrix protein (porin) of Escherichia coli. *Biochim. Biophys. Acta* **511**, 305–19 (1978).
  43. Montal, M. & Mueller, P. Formation of bimolecular membranes from lipid monolayers and a study of their electrical properties. *Proc. Natl. Acad. Sci. U. S. A.* **69**, 3561–6 (1972).
  44. Eswar, N. *et al.* Comparative Protein Structure Modeling With MODELLER. *Curr. Protoc. Bioinforma.* **15**, 5.6.1–5.6.30 (2006).
  45. Sali, A. & Blundell, T. L. Comparative protein modelling by satisfaction of spatial restraints. *J. Mol. Biol.* **234**, 779–815 (1993).
  46. Phillips, J. C. *et al.* Scalable molecular dynamics with NAMD. *J. Comput. Chem.* **26**, 1781–1802 (2005).
  47. Harvey, M., Giupponi, G. & De Fabritiis, G. ACEMD: Accelerating Biomolecular Dynamics in the Microsecond Time Scale. *J. Chem. Theory Comput.* **5**, 1632–1639 (2009).
  48. Sindhikara, D. J., Kim, S., Voter, A. F. & Roitberg, A. E. Bad Seeds Sprout Perilous Dynamics: Stochastic Thermostat Induced Trajectory Synchronization

- in Biomolecules. *J. Chem. Theory Comput.* **5**, 1624–1631 (2009).
49. Lindorff-Larsen, K. *et al.* Improved side-chain torsion potentials for the Amber ff99SB protein force field. *Proteins* **78**, 1950–1958 (2010).
  50. Jorgensen, W., Chandrasekhar, J., Madura, J., Impey, R. & Klein, M. Comparison of simple potential functions for simulating liquid water. *J. Chem. Phys.* **79**, 926–936 (1983).
  51. Kumar, A., Hajjar, E., Ruggerone, P. & Ceccarelli, M. Structural and dynamical properties of the porins OmpF and OmpC: insights from molecular simulations. *J. Phys. Condens. matter* **22**, 454125 (2010).
  52. Kyte, J. & Doolittle, R. F. A simple method for displaying the hydrophobic character of a protein. *J. Mol. Biol.* **157**, 105–132 (1982).
  53. Mezei, M. Simulaid: A simulation facilitator and analysis program. *J. Comput. Chem.* **31**, 2658–2668 (2010).
  54. Baker, N. A., Sept, D., Joseph, S., Holst, M. J. & McCammon, J. A. Electrostatics of nanosystems: application to microtubules and the ribosome. *Proc. Natl. Acad. Sci. U. S. A.* **98**, 10037–10041 (2001).
  55. Humphrey, W., Dalke, A. & Schulten, K. VMD: visual molecular dynamics. *J. Mol. Graph. Model.* **14**, 33–38 (1996).
  56. Dolinsky, T. J., Nielsen, J. E., McCammon, J. A. & Baker, N. A. PDB2PQR: an automated pipeline for the setup of Poisson-Boltzmann electrostatics calculations. *Nucleic Acids Res.* **32**, 665–667 (2004).
  57. Dolinsky, T. J. *et al.* PDB2PQR: expanding and upgrading automated preparation of biomolecular structures for molecular simulations. *Nucleic Acids Res.* **35**, 522–525 (2007).
  58. Li, H., Robertson, A. D. & Jensen, J. H. Very fast empirical and rationalization

- of protein pKa values. *Proteins* **61**, 704–721 (2005).
59. Im, W. & Roux, B. Ion Permeation and Selectivity of OmpF Porin: A Theoretical Study Based on Molecular Dynamics, Brownian Dynamics, and Continuum Electrodiffusion Theory. *J. Mol. Biol.* **322**, 851–869 (2002).
  60. Grantham, R. Amino acid difference formula to help explain protein evolution. *Science* **185**, 862–4 (1974).
  61. Muñoz, V. & Serrano, L. Elucidating the folding problem of helical peptides using empirical parameters. *Nat. Struct. Biol.* **1**, 399–409 (1994).
  62. Muñoz, V. & Serrano, L. Development of the multiple sequence approximation within the AGADIR model of alpha-helix formation: comparison with Zimm-Bragg and Lifson-Roig formalisms. *Biopolymers* **41**, 495–509 (1997).
  63. Lacroix, E., Viguera, A. R. & Serrano, L. Elucidating the folding problem of alpha-helices: local motifs, long-range electrostatics, ionic-strength dependence and prediction of NMR parameters. *J. Mol. Biol.* **284**, 173–91 (1998).
  64. Case, D. A. *et al.* Amber 14. (2014).
  65. Fukunishi, H., Watanabe, O. & Takada, S. On the Hamiltonian replica exchange method for efficient sampling of biomolecular systems: Application to protein structure prediction. *J. Chem. Phys.* **116**, 9058 (2002).
  66. Kannan, S. & Zacharias, M. Enhanced sampling of peptide and protein conformations using replica exchange simulations with a peptide backbone biasing-potential. *Proteins* **66**, 697–706 (2007).
  67. Sugita, Y. & Okamoto, Y. Replica-exchange molecular dynamics method for protein folding. *Chem. Phys. Lett.* **314**, 141–151 (1999).
  68. Bergonzo, C. *et al.* Multidimensional Replica Exchange Molecular Dynamics Yields a Converged Ensemble of an RNA Tetranucleotide. *J. Chem. Theory*

- Comput.* **10**, 492–499 (2014).
69. Kabsch, W. & Sander, C. Dictionary of protein secondary structure: pattern recognition of hydrogen-bonded and geometrical features. *Biopolymers* **22**, 2577–637 (1983).
  70. Sreerama, N. & Woody, R. W. A self-consistent method for the analysis of protein secondary structure from circular dichroism. *Anal. Biochem.* **209**, 32–44 (1993).
  71. Greenfield, N. & Fasman, G. D. Computed circular dichroism spectra for the evaluation of protein conformation. *Biochemistry* **8**, 4108–16 (1969).
  72. Wishart, D. S., Sykes, B. D. & Richards, F. M. Relationship between nuclear magnetic resonance chemical shift and protein secondary structure. *J. Mol. Biol.* **222**, 311–33 (1991).
  73. Wishart, D. S., Sykes, B. D. & Richards, F. M. The chemical shift index: a fast and simple method for the assignment of protein secondary structure through NMR spectroscopy. *Biochemistry* **31**, 1647–51 (1992).
  74. Wishart, D. S. & Sykes, B. D. The <sup>13</sup>C chemical-shift index: a simple method for the identification of protein secondary structure using <sup>13</sup>C chemical-shift data. *J. Biomol. NMR* **4**, 171–80 (1994).
  75. Miles, A. J. & Wallace, B. A. Synchrotron radiation circular dichroism spectroscopy of proteins and applications in structural and functional genomics. *Chem. Soc. Rev.* **35**, 39–51 (2006).
  76. De Pinto, V. *et al.* Determination of the Conformation of the Human VDAC1 N-Terminal Peptide , a Protein Moiety Essential for the Functional Properties of the Pore. *Chembiochem* **8**, 744–756 (2007).
  77. Strandberg, E. & Ulrich, A. S. NMR methods for studying membrane-active

- antimicrobial peptides. *Concepts Magn. Reson. Part A* **23A**, 89–120 (2004).
78. Manzo, G. *et al.* Toward an improved structural model of the frog-skin antimicrobial peptide esculentin-1b(1-18). *Biopolymers* **97**, 873–81 (2012).
79. Scorciapino, M. A. *et al.* A novel dendrimeric peptide with antimicrobial properties: structure-function analysis of SB056. *Biophys. J.* **102**, 1039–48 (2012).
80. Crevenna, A. H., Naredi-Rainer, N., Lamb, D. C., Wedlich-Söldner, R. & Dzubiella, J. Effects of Hofmeister ions on the  $\alpha$ -helical structure of proteins. *Biophys. J.* **102**, 907–15 (2012).
81. Barth, A. Infrared spectroscopy of proteins. *Biochim. Biophys. Acta - Bioenerg.* **1767**, 1073–1101 (2007).
82. Amodeo, G. F., Scorciapino, M. A., Messina, A., De Pinto, V. & Ceccarelli, M. Charged residues distribution modulates selectivity of the open state of human isoforms of the voltage dependent anion-selective channel. *PLoS One* **9**, (2014).
83. Lide, D. R. *CRC Handbook of Chemistry and Physics*. (Taylor and Francis, 2007).
84. Tomasello, F. M., Guarino, F., Reina, S., Messina, A. & De Pinto, V. The voltage-dependent anion selective channel 1 (VDAC1) topography in the mitochondrion outer membrane as detected in intact cell. *PLoS One* **8**, e81522 (2013).
85. Song, J., Midson, C., Blachly-dyson, E., Forte, M. & Colombini, M. The Sensor Regions of VDAC Are Translocated from within the Membrane to the Surface during the Gating Processes. *Biophys. J.* **74**, 2926–2944 (1998).
86. Schneider, R. *et al.* The Native Conformation of the Human VDAC1 N

- Terminus \*\*. *Angew. Chemie Int. Ed.* **49**, 1882–1885 (2010).
87. Reina, S. *et al.* Swapping of the N-terminus of VDAC1 with VDAC3 restores full activity of the channel and confers anti-aging features to the cell. *FEBS Lett.* **584**, 2837–2844 (2010).
  88. Villinger, S. *et al.* Functional dynamics in the voltage-dependent anion channel. *Proc. Natl. Acad. Sci. U. S. A.* **107**, 22546–22551 (2010).
  89. Reina, S. *et al.* Deletion of b-strands 9 and 10 converts VDAC1 voltage-dependence in an asymmetrical process. *Biochim. Biophys. Acta* **1827**, 793–805 (2013).
  90. Maurya, S. R. & Mahalakshmi, R. Modulation of human mitochondrial voltage-dependent anion channel 2 (hVDAC2): structural stability by cysteine-assisted barrel-lipid interactions. *J. Biol. Chem.* **288**, 25584–25592 (2013).
  91. Yehezkel, G., Abu-hamad, S. & Shoshan-Barmatz, V. An N-Terminal Nucleotide-Binding Site in VDAC1 : Involvement in Regulating Mitochondrial Function. *J. Cell. Physiol.* **212**, 551–561 (2007).
  92. Guo, X. W. *et al.* Molecular Design of the Voltage-Dependent, Anion-Selective Channel in the Mitochondrial Outer Membrane. *J. Struct. Biol.* **114**, 41–59 (1995).
  93. Colombini, M. VDAC structure, selectivity, and dynamics. *Biochim. Biophys. Acta* **1818**, 1457–65 (2012).
  94. Menzel, V. A. *et al.* Molecular and functional characterization of VDAC2 purified from mammal spermatozoa. *Biosci. Rep.* **29**, 351–362 (2009).
  95. Krammer, E.-M., Homblé, F. & Prévost, M. Molecular origin of VDAC selectivity towards inorganic ions: a combined molecular and Brownian dynamics study. *Biochim. Biophys. Acta* **1828**, 1284–92 (2013).

96. Xu, X., Decker, W., Sampson, M. J., Craigen, W. J. & Colombini, M. Mouse VDAC Isoforms Expressed in Yeast: Channel Properties and Their Roles in Mitochondrial Outer Membrane Permeability. *J. Membr. Biol.* **170**, 89–102 (1999).
97. Krammer, E.-M., Homblé, F. & Prévost, M. Concentration dependent ion selectivity in VDAC: a molecular dynamics simulation study. *PLoS One* **6**, e27994 (2011).
98. Lee, K. Il, Rui, H., Pastor, R. W. & Im, W. Brownian dynamics simulations of ion transport through the VDAC. *Biophys. J.* **100**, 611–619 (2011).
99. Gattin, Z. *et al.* Solid-state NMR, electrophysiology and molecular dynamics characterization of human VDAC2. *J. Biomol. NMR* **61**, 311–20 (2015).
100. Rostovtseva, T. K. & Bezrukov, S. M. ATP Transport Through a Single Mitochondrial Channel , VDAC , Studied by Current Fluctuation Analysis. *Biophys. J.* **74**, 2365–2373 (1998).